AGU PUBLICATIONS

JGR

Journal of Geophysical Research: Atmospheres

RESEARCH ARTICLE
10.1002/2014JD022961

Special Section:
The 2011-12 Indian Ocean Field Campaign: Atmospheric-Oceanic Processes and MJO Initiation

Effect of dry large-scale vertical motions on initial MJO convective onset

Scott W. Powell[1] **and Robert A. Houze Jr.**[1]

[1]Department of Atmospheric Sciences, University of Washington, Seattle, Washington, USA

Abstract Anomalies of eastward propagating large-scale vertical motion with ~30 day variability at Addu City, Maldives, move into the Indian Ocean from the west and are implicated in Madden-Julian Oscillation (MJO) convective onset. Using ground-based radar and large-scale forcing data derived from a sounding array, typical profiles of environmental heating, moisture sink, vertical motion, moisture advection, and Eulerian moisture tendency are computed for periods prior to those during which deep convection is prevalent and those during which moderately deep cumulonimbi do not form into deep clouds. Convection with 3–7 km tops is ubiquitous but present in greater numbers when tropospheric moistening occurs below 600 hPa. Vertical eddy convergence of moisture in shallow to moderately deep clouds is likely responsible for moistening during a 3–7 day long transition period between suppressed and active MJO conditions, although moistening via evaporation of cloud condensate detrained into the environment of such clouds may also be important. Reduction in large-scale subsidence, associated with a vertical velocity structure that travels with a dry eastward propagating zonal wavenumbers 1–1.5 structure in zonal wind, drives a steepening of the lapse rate below 700 hPa, which supports an increase in moderately deep moist convection. As the moderately deep cumulonimbi moisten the lower troposphere, more deep convection develops, which itself moistens the upper troposphere. Reduction in large-scale subsidence associated with the eastward propagating feature reinforces the upper tropospheric moistening, helping to then rapidly make the environment conducive to formation of large stratiform precipitation regions, whose heating is critical for MJO maintenance.

Key Points:
- A dry wavenumber 1 zonal wind and vertical velocity MJO signal is shown
- Large-scale reduction in subsidence instrumental in DYNAMO MJO onset

Correspondence to:
S. W. Powell,
spowell@atmos.uw.edu

Citation:
Powell, S. W., and R. A. Houze Jr. (2015), Effect of dry large-scale vertical motions on initial MJO convective onset, *J. Geophys. Res. Atmos.*, *120*, 4783–4805, doi:10.1002/2014JD022961.

Received 9 DEC 2014
Accepted 21 APR 2015
Accepted article online 24 APR 2015
Published online 27 MAY 2015
Corrected 1 JUL 2015

This article was corrected on 1 JUL 2015. See the end of the full text for details.

©2015. American Geophysical Union. All Rights Reserved.

1. Introduction

In its moist, convective form, the Madden-Julian Oscillation (MJO) [*Madden and Julian*, 1971, 1972; *Zhang*, 2005] is characterized by a widespread area of deep, organized, and eastward propagating convection that develops between the central equatorial Indian Ocean and tropical west Pacific. While many have invoked extratropical influences into MJO convective initiation [e.g., *Hsu et al*., 1990; *Ray and Li*, 2013; *Zhao et al*., 2013], several studies have suggested that tropical dynamics influence the formation of MJO convection. *Knutson and Weickmann* [1987] first showed that anomalies of velocity potential centered in the tropics circumnavigated the globe at upper levels and were coincident with onset of at least some MJO events. The anomalies were dominated by the zonal wind component of an eastward propagating wavenumber 1 feature. Other studies have since shown that such circumnavigating features are present in individual cases [e.g., *Matthews*, 2008; *Gottschalck et al*., 2013; *Straub*, 2013], while some have shown the same in composites of several MJO events [e.g., *Seo and Kim*, 2003; *Kiladis et al*., 2005; *Straub*, 2013; *Adames and Wallace*, 2014a]. Upper tropospheric velocity potential can even be used in indices to identify past and ongoing MJO events [*Ventrice et al*., 2013; *Adames and Wallace*, 2014a] or predict future ones.

Bladé and Hartmann [1993] did not rule out that circumnavigating features could sometimes influence the formation of new MJO convection; however, they considered that no clear concurrent dynamical relationship exists between upper tropospheric velocity potential anomalies and generation of convection in the lower troposphere. They proposed a mechanism (known as "discharge-recharge") through which the variable frequency of the MJO was set by the period of conditional instability of the second kind [e.g., *Charney and Elliasen*, 1964] buildup associated with an increase in sea surface temperature. The idea was more recently extended to the buildup of tropospheric moist static energy and moisture as seen in *Kemball-Cook and Weare* [2001] and *Benedict and Randall* [2007]. They argue that clouds gradually become deeper over a period of several weeks as they slowly humidify the troposphere from the surface upward; then, at the end of the multiweek period, the environment allows enough deeper convection to support an MJO convective event. However *Powell and Houze* [2013] (hereafter PH13) show that the time scale of

such a proposed feedback process was not evident in radar and rawinsonde observations made during the Dynamics of the Madden-Julian Oscillation (DYNAMO) and Atmospheric Radiation Measurement Madden-Julian Oscillation Investigation Experiment (AMIE) in 2011–2012. Instead, they observed that an increase in depth of convection occurred on a shorter time scale near the beginning of a large-scale convective event. *Powell and Houze* [2015] reached the same conclusions for a larger spatial domain by using satellite-based radar data. Moreover, several episodes of deep convection, building and decaying on time scales shorter than the MJO time scale, occur during an active period of an MJO [*Zuluaga and Houze*, 2013]. Either discharge-recharge is not a valid hypothesis and a different mechanism is responsible for MJO onset or its processes occur more quickly than previously thought.

Modeling studies have supported the idea that deep convection is most sensitive to humidity in the lower half of the troposphere. Using two cloud-resolving models, *Derbyshire et al*. [2004] demonstrated that upward in-cloud mass flux was dramatically reduced above a level at and above which they set relative humidity to less than 50%, although their study was specifically aimed at testing the sensitivity of convection to midtropospheric humidity. *Wang and Sobel* [2012] imposed drying in a cloud-resolving model approaching weak temperature gradient equilibrium. They showed that simulated precipitation was sensitive to drying below 8 km and that as their model approaches equilibrium, a wide range of precipitation values was present when drying was imposed below 8 km for a narrow range of column-integrated humidity. More recent evidence shows that global models using cumulus parameterizations do not accurately represent the observed wide-ranging distribution of precipitation that occurs where total precipitable water is greater than 50 mm (D. Kim, personal communication). In other words, ample low and midtropospheric humidity appears to be a necessary but insufficient condition for deep convection to occur. Furthermore, even if deep convection develops, there is no evidence that it can organize into the large mesoscale system characteristic of the MJO in the presence of strong middle to upper tropospheric drying.

Both past and contemporary studies have highlighted the importance of large-scale motions in impacting formation of deep convection in the tropics. *Yanai et al*. [1976] showed that mass fluxes in deeper clouds correlate strongly with large-scale vertical motion at their detrainment levels. They concluded that upper tropospheric vertical motion had a "controlling influence" on deep clouds, which they hypothesized would happen because large-scale ascent would cause cooling that would destabilize the tropospheric stratification. In the tropics, *Jensen and Del Genio* [2006] concluded that rather than a stable layer at the 0°C level, midtropospheric drying associated with subsidence is likely responsible for limiting the echo top heights of cumulus congestus clouds, which are precursor cloud elements to eventual formation of deep convection, and eventually, larger mesoscale convective systems (MCSs). *Takayabu et al*. [2010] demonstrated that deep layer latent heating in the troposphere is hindered by large-scale subsidence, although precipitation can fall from shallow clouds or congestus clouds under that condition. They noted that even where sea surface temperatures exceed 28°C, large-scale subsidence suppresses deep convection. *Hohenegger and Stevens* [2013] argued that the time scale for cumulus congestus to grow into deep convection is smaller than the time required for congestus to moisten the troposphere. Furthermore, they showed that the likelihood of a congestus cloud growing into a deep cumulonimbus cloud does not increase with longer congestus life times. They stated that "deep convection is triggered because of some form of imposed ascent." More recently, *Kumar et al*. [2013, 2014] have shown how large-scale vertical motions impact the modal depth of convection in a hybrid maritime/continental environment near Darwin, Australia. *Kumar et al*. [2014] demonstrated that substantially greater than average large-scale upward motion, and thus greater vertical advection of moisture, is present when the majority of moderately deep clouds grow into deep cumulonimbus clouds. Furthermore they showed that the ability for cumulus clouds that are 3–7 km deep to grow into deep cumulonimbi (top $>$ 9 km) is not dependent upon the number of such clouds present. They rejected the hypothesis that congestus-type cumuli or cumulonimbi are responsible for moistening prior to formation of deep cumulonimbi. Neither study, however, directly applies to the potential time scale of large-scale convective buildup as seen with MJO cases, but rather they focus on the growth of individual clouds, which occurs on much smaller time scales. For the MJO cases observed during DYNAMO, *Ruppert and Johnson* [2015] have shown that the reduction of large-scale subsidence coincided with low to middle tropospheric moistening prior to MJO convective onset. They concluded that reduction in large-scale subsidence combined with convective moistening to trigger MJO onset. They also supported a conclusion of *Sobel et al*. [2014] that drying by horizontal

advection decreased while increased upward vertical moisture advection occurred in the days prior to MJO onset. Consistent with this, other studies [e.g., *Sobel et al*., 2014; *Johnson et al*., 2015; *Ruppert and Johnson*, 2015] have shown that a reduction in radiative cooling occurs in the troposphere prior to MJO onset.

The primary goal of this article is to explore a potential role of large-scale upper tropospheric dynamic features observed over the Indian Ocean during DYNAMO/AMIE in the development of several observed eastward propagating large-scale convective events (LCEs). At a single location in the equatorial Indian Ocean, PH13 noted a regular period in the anomalies of zonal wind at 150 hPa and temperature and humidity between about 500 and 200 hPa. Whether the anomalies were caused by deep convection or existed elsewhere prior to the formation of deep convection was not determinable from rawinsonde data at a single location. However, studies such as *Gottschalck et al*. [2013] showed that velocity potential anomalies at 200 hPa, which were dominated by zonal wind anomalies, propagated into the Indian Ocean from the west during DYNAMO. Therefore, the onset of convection may have been related to associated favorable anomalous large-scale vertical motions propagating into the region.

We focus on the initial onset of MJO-related convection, which during the cases observed during DYNAMO/AMIE, occurred over the central Indian Ocean. We will relate deep large-scale vertical motion anomalies with development and suppression of deep convection and MCSs associated with each MJO event occurring between October 2011 and March 2012 over the Indian Ocean. We will proceed by

1. Calculating large-scale vertical motions in the upper troposphere and documenting whether anomalous vertical motions propagate eastward around the globe,
2. Revealing the zonal structure through the depth of the troposphere of any such vertical motion anomalies and zonal wind anomalies,
3. Determining, as in *Kumar et al*. [2014], vertical profiles of temperature and water vapor during periods when moderately deep (3–7 km) cumulonimbi do and do not grow into deep cumulonimbi, and
4. Exploring whether motions obtained in (1) and (2) were sufficient to have supported deep cumulonimbus formation over the Indian Ocean based on results from (3).

2. Data and Reanalysis

Global structures of velocity potential, upper tropospheric divergence, vertical motion, and zonal wind are determined using ECMWF Re-Analysis (ERA)-Interim reanalysis (ERA-I) [*Dee et al*., 2011] at 6 h temporal resolution. The seasonal cycle is first removed from all model fields used by removing the annual average and the first three harmonics using a composite of reanalysis data from 1979 to 2011. Anomalies are then calculated relative to the mean of the resulting fields from 1 August to 31 March.

Radar data used in section 5 is from the S-band radar of the National Center for Atmospheric Research S-PolKa system at 0.63°S, 73.10°E. Specifically, we use range-height indicator (RHI) scans (an RHI scan being defined as a continuous scan of the antenna elevation angle upward or downward while pointing in a constant azimuthal direction) in the northeastern quadrant of the region of radar coverage. Spacing between recorded elevation angle data for RHIs was 0.5°, the lowest elevation angle was 0.5°, and the highest elevation angle was 41°. The resulting high vertical resolution allows for accurate estimations of echo top heights for precipitating elements. The temporal resolution of the RHI volumes was 15 min, and the data were recorded in range bins of 150 m out to a maximum range of 150 km. Data were collected from 1 October 2011 to 15 January 2012.

Rawinsonde data used in section 5 are from Gan (0.69°S, 73.15°E) in Addu City, Maldives. Their temporal resolution was 3 h, and data were interpolated to 5 hPa vertical resolution. Details about quality control of the sounding data are available in *Long and Holdridge* [2012]. Relative humidity at and above the 0°C level is shown in this paper with respect to ice. The rawinsonde-derived large-scale forcing data set employed in section 5 is that from *Ciesielski et al*. [2014] and *Johnson et al*. [2015]. The data set is gridded to 1° horizontal and 25 hPa vertical resolution and covers most of the Indian Ocean. In this study, the gridded data set supplements the sounding observations with original analysis from the European Centre for Medium-Range Weather Forecasting (ECMWF) model. The data set and further details about it are available at http://johnson.atmos.colostate.edu/dynamo/products/gridded/index.html. The intraseasonal variability in convection and tropospheric structure observed within spatially limited radar and rawinsonde

data sets has been shown to be consistent with the same over a much larger domain spanning much of the equatorial Indian Ocean [*Powell and Houze*, 2015]. They also showed that the time scale required for the distribution of precipitating clouds to transition from moderately deep congestus to deep cumulonimbi prior to MJO convective onset, as observed by S-PolKa, was consistent with that on the large scale.

Precipitation rates are derived from rainfall estimates of the version-7 3B42 products [*Huffman et al*., 2007], which are generated using data from the Tropical Rainfall Measuring Mission (TRMM) satellite [*Kummerow et al*., 1998] and other satellite platforms. Details about the 3B42 algorithm can be found at ftp://meso-a.gsfc.nasa.gov/pub/trmmdocs/3B42_3B43_doc.pdf. Figure 1 is a time-longitude diagram of the precipitation rain rates averaged between 3°N and 3°S. The solid black vertical line in this and later figures of this format highlights the longitude of Gan. Along the vertical line are black marks that mark the dates of the first MCSs observed via ground-based precipitation radar in Addu City (see section 4 of PH13) during large-scale convective events (LCEs) in October (LCE1), November (LCE2), and December (LCE3). Those dates are 16 October, 18 November, and 15 December. (Radar domain averaged precipitation that was not stratiform in nature but was in excess of 3 mm d^{-1} was observed as early as 12 November near the beginning of LCE2.) The ground-based radars were inactive after 9 February. Increased precipitation also occurred over the equatorial Indian Ocean in late February and March, and this event is henceforth referred to as LCE5. A January event, which was located away from the equator but seen in TRMM data by *Yoneyama et al*. [2013], will be referred to as LCE4. Precipitation in much of the equatorial Western Hemisphere was near zero before February; more precipitation was observed after 1 February as the Intertropical Convergence Zone over South America and the Atlantic Ocean moved southward.

3. Velocity Potential Anomalies at 150 hPa

Convection associated with the MJO during DYNAMO/AMIE was usually located within 5–10° of latitude of the equator [*Yoneyama et al*., 2013]. Furthermore, outgoing longwave radiation (OLR) regressed onto the first two principal components (PCs) of the $\Delta\chi$ (Laplacian of velocity potential) field yield structures that extend to about 10–15° of latitude [*Adames and Wallace*, 2014a]. Primarily because of the latter, methods of tracking the zonal propagation [e.g., *Wheeler and Weickmann*, 2001] of mean near-equatorial OLR or zonal wind anomalies typically average such fields between 10° and 10°S. However, the leading edge of zonal wind structures as they enter the Indian Ocean may be restricted to very close to the equator [*Adames and Wallace*, 2014a; *Haertel et al*., 2014]. If the leading edges of the zonal wind anomalies are dynamically important for MJO convective onset, then identification and prediction of MJO events in general may benefit from considering averages of relevant fields over a narrow range of latitude near the equator. Therefore, all time-longitude Hovmöller diagrams in this paper are averaged between 3°N and 3°S.

Figure 2 shows the progression of 150 hPa velocity potential anomalies (χ_{150}'), which are derived from ERA-I, through the near-equatorial region between 1 September 2011 and 31 March 2012. White dots scattered throughout the figure align longitudinally with the minimum of χ_{150}' at each time. *Gottschalck et al*. [2013] showed similar figures for the 200 hPa level; however, because zonal wind anomalies during DYNAMO/AMIE were stronger at 150 hPa (Figure 7 in PH13), and coherence between the first two PCs of the velocity potential signal at 150 hPa is slightly more coherent than that at 200 hPa [*Adames and Wallace*, 2014a], we use velocity potential at 150 hPa. The gradient of the velocity potential is the vector divergent wind field, and the Laplacian of the velocity potential represents the divergence. The velocity potential effectively represents the gravest modes of divergence present at a given pressure level, such that negative velocity potential is indicative of large-scale divergence [e.g., *Lorenc*, 1984; *Hendon*, 1986]. PH13 showed that zonal wind anomalies with variability of ~30 days dominated the vector wind anomalies on the same time scale; therefore, the χ_{150}' field was mostly a consequence of the 150 hPa zonal wind anomaly.

Velocity potential anomalies were negative near Gan at the beginning of September and were probably associated with heightened convective activity over the Indian Ocean during late August and early September. Positive velocity potential anomalies were located to the west of the negative anomalies at the same time. The negative (positive) anomalies were present near the date line between 15 September and 4 October (4 October and 3 November). The χ_{150}' was positive over Gan between 21 September and 15 October. Positive χ_{150}' clearly continued eastward past the date line; however, it is not clear whether the negative anomaly also propagated past the date line. Nonetheless, a region of negative χ_{150}' with a

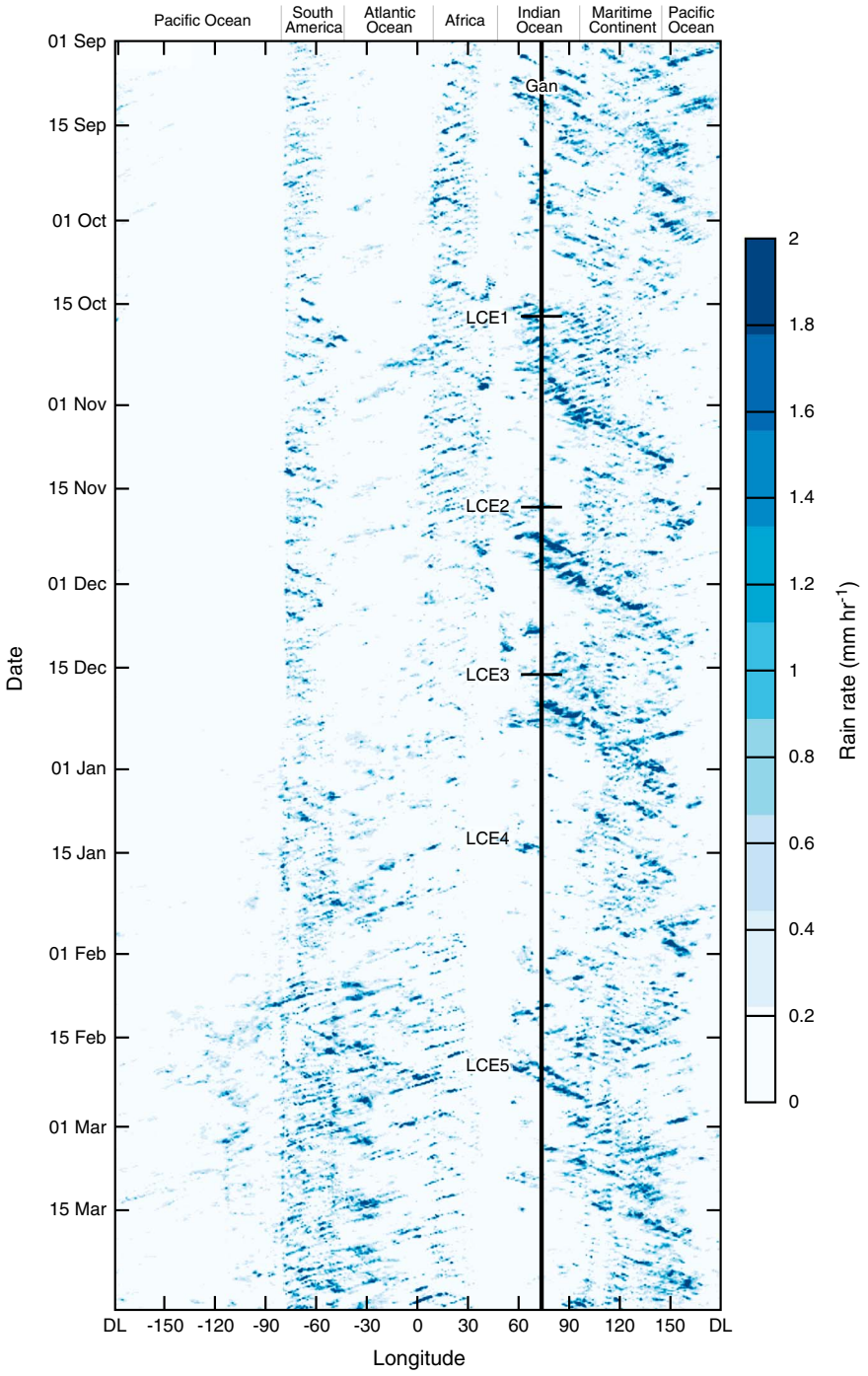

Figure 1. Time-longitude diagram of estimated rainfall rate using the TRMM 3B42 product from 1 September 2011 to 31 March 2012. Data are degraded to 0.75°×0.75° resolution and are averaged between 3°N and 3°S. The vertically oriented, solid, black line represents the longitude of Gan. The horizontally oriented black marks along the vertical black line represent the dates on which the first MCS was observed by radar during LCEs 1–3.

longitudinal width of 90 to 120° over South America and the Atlantic propagated eastward into the Indian Ocean, and the velocity potential anomaly became negative at Gan on 15 October. The negative anomaly then repeatedly circumnavigated the globe, again reaching Gan on 15 November and 15 December. The negative anomaly cannot be distinctly traced again beyond the date line, although negative anomalies propagated eastward from the central Pacific separately in early and mid-January, with intermittent

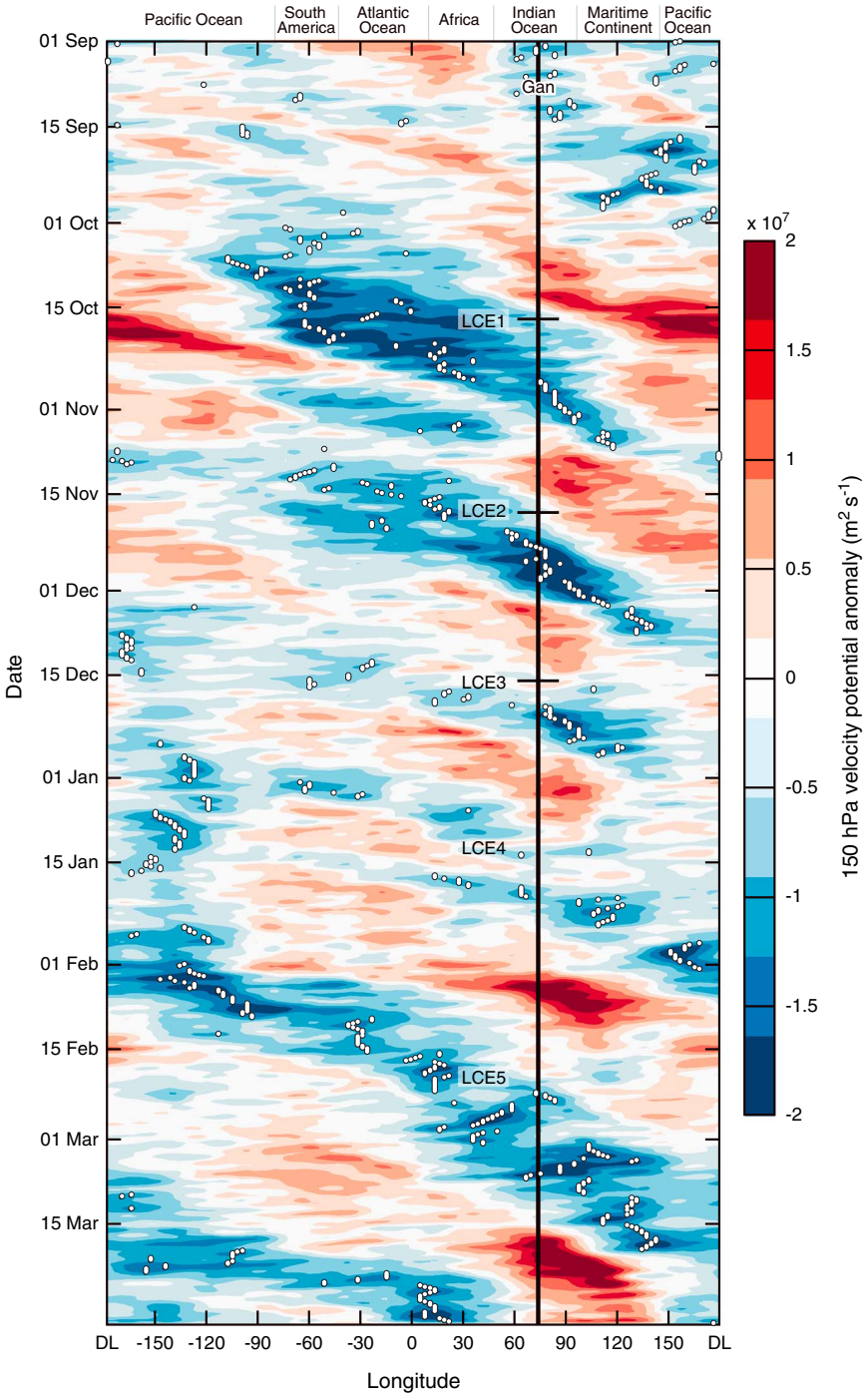

Figure 2. Time-longitude diagram of 150 hPa velocity potential (χ) anomaly derived from ERA-I averaged from 3°N to 3°S. See Figure 1 for description of black lines and marks. The white dots at each time represent the longitude of the minimum velocity potential anomaly.

negative χ_{150}' occurring over Gan in January. The negative anomaly further tracked around the globe again until it reached Gan on 15 February. It then continued to propagate off to the east and was situated over the Atlantic and Africa by the end of March.

If the negative anomaly over the Indian Ocean in September connected to the negative anomaly that subsequently propagated around the globe during October, then the October LCE was likely a successive event directly linked to the precipitation event there in August and September. *Yoneyama et al.* [2013]

articulated the same idea. (See *Matthews* [2008] for a description of primary and successive MJO events.) LCE2 is clearly linked through the χ_{150}' field to LCE1 as is LCE3 to LCE2. The negative χ_{150}' anomalies present over the Indian Ocean during middle to late January appear to be directly connected to those over the Indian Ocean in middle to late December as are the same anomalies detected over the Indian Ocean in February and March to the ones seen in January. One could argue based on the propagation of the negative velocity potential anomaly that all of the extended periods of negative χ_{150}' over Gan might be attributed to the same velocity potential anomaly that continually propagated around the globe during DYNAMO/AMIE. This interpretation is further supported below when we highlight the low-frequency component of large-scale vertical motion associated with the χ_{150} field. Because the first negative velocity potential anomalies preceded by 1–2 days the first MCS formation associated with LCEs 1 and 2 at Gan and correspond closely with the MCS development at the start of LCE3, a physical relationship between the arrival of negative velocity potential in the upper troposphere and formation of persistent deep convection over the Indian Ocean is suspected just as it originally was by *Knutson and Weickmann* [1987].

4. Vertical Velocity and Zonal Wind Structures

4.1. Time-Longitude Diagrams of Vertical Velocity Anomalies

Because the tropopause can be approximated as a rigid lid for most tropospheric motions, a negative velocity potential anomaly, or positive large-scale divergence anomaly, in the upper troposphere must then be associated with anomalous upward motion below. Figure 3 depicts the 300 hPa vertical velocity (ω) fields derived from ERA-I. Within 3° longitude and latitude of Gan, divergence, smoothed with a 4 day running mean, at 200 hPa is strongly correlated with vertical motion, also smoothed, at 300 hPa (correlation coefficient $\rho = -0.86$; 95% confidence interval: $-0.61 \geq \rho \geq -0.95$). Similarly high correlations existed throughout the tropics. Frequent ω of -0.2 to $-0.3\ \mathrm{Pa\,s^{-1}}$ occurred over the Indian Ocean and Maritime Continent during convectively active periods, particularly in October–December. Eastward propagating streaks of ω with magnitudes as large as $-0.5\ \mathrm{Pa\,s^{-1}}$ can probably be attributed to high-wavenumber Kelvin waves [*Johnson and Ciesielski*, 2013; *DePasquale et al.*, 2014]. No coherent ω structures appear that are associated with the velocity potential anomaly that propagated through the Indian Ocean in late January. Upward motion at 300 hPa between 75°W and 30°E after 1 February is associated at least partially with increased latent heating (inferred from enhanced precipitation associated with the southward shift of the Intertropical Convergence Zone; Figure 1) during that period. The strongest upward motions shown in Figure 3 are constrained to regions and times where the greatest amounts of precipitation are known to have fallen (Figure 1). Recall that all values described here are representative only of motions within a model grid point. Actual vertical velocities on the subgrid scale are bound to locally exceed the values shown in Figure 3 in some locations and perhaps have opposite sign in others.

In nature, divergence and vertical velocity are both highly variable in space and time. The velocity potential field contains information about both the low and high-frequency variability in the divergence field; however, the low-frequency component of divergence contributes strongly to its total and the Laplacian of its smoothed field yields large-scale structures of divergence. Smoothing the global divergence and vertical velocity fields to suppress their high-frequency signals thus reveals the large-scale structures associated with most of the total velocity potential. Details about the smoothing technique used are provided in Appendix A. We first smooth vertical velocity so that the magnitude of the resulting field at all grid points was, globally, a median of 90% of the original field's magnitude. Doing so, we obtained fields that represent large-scale divergence and vertical velocity. By setting $\sigma_x = 27$ and $\sigma_y = 13$ (see Appendix A for definitions of variables), we only suppress signals with zonal (meridional) wavelength less than 120° (60°). Resulting signals are therefore spatially smaller, both zonally and meridionally, than the size of the zonal wind or vertical velocity fields associated with the MJO as documented by *Adames and Wallace* [2014a, 2014b]. The Hovmöller for smoothed vertical velocity anomalies (ω') is given in Figure 4, and the white dots represent the 150 hPa velocity potential minima using the same smoothing as used on 300 hPa ω. Sustained anomalous large-scale upward motion began at Gan at 300 hPa on 15 October, 17 November, 13 December, 12 January, and 12 February. Westward propagating negative anomalies of ω also moved into the Indian Ocean from the tropical west Pacific between LCE2 and LCE3, between LCE3 and LCE4, and between LCE4 and LCE5. The westward propagating anomalies even appeared to reach Gan a few days

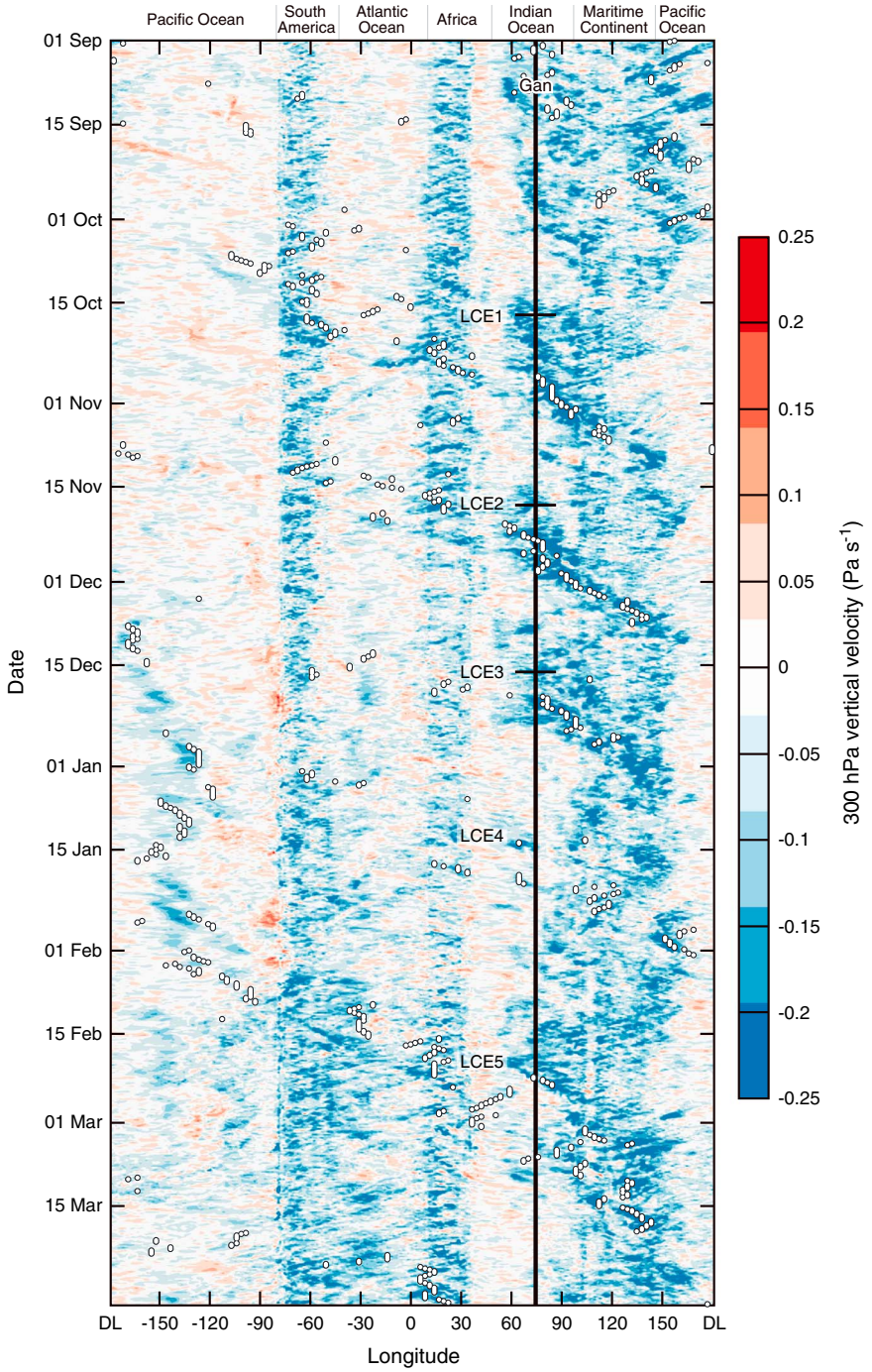

Figure 3. Same as Figure 2 but with color contours for 300 hPa ω.

before the eastward propagating circumnavigating anomalies prior to LCE5. Smoothed ω' throughout the tropics was usually less than 0.05 Pa s^{-1} in magnitude and between 0.01 and 0.03 Pa s^{-1} in the Western Hemisphere, where widespread, deep convection at the equator was less prevalent.

A stronger low-pass filter (i.e., more smoothing) more clearly depicts circumnavigating behavior of large-scale vertical velocity anomalies. The extrema of the first two PCs of $\Delta\chi$ were noted by *Adames and Wallace* [2014a] to be separated by 120° longitude. A latitudinal half width of 22.5° closely corresponds to the width of the anomalous zonal wind signal in ERA-I (not shown) and contains the vertical velocity signal regressed onto the first two PCs of $\Delta\chi$ as described by *Adames and Wallace* [2014b]. For such a filter,

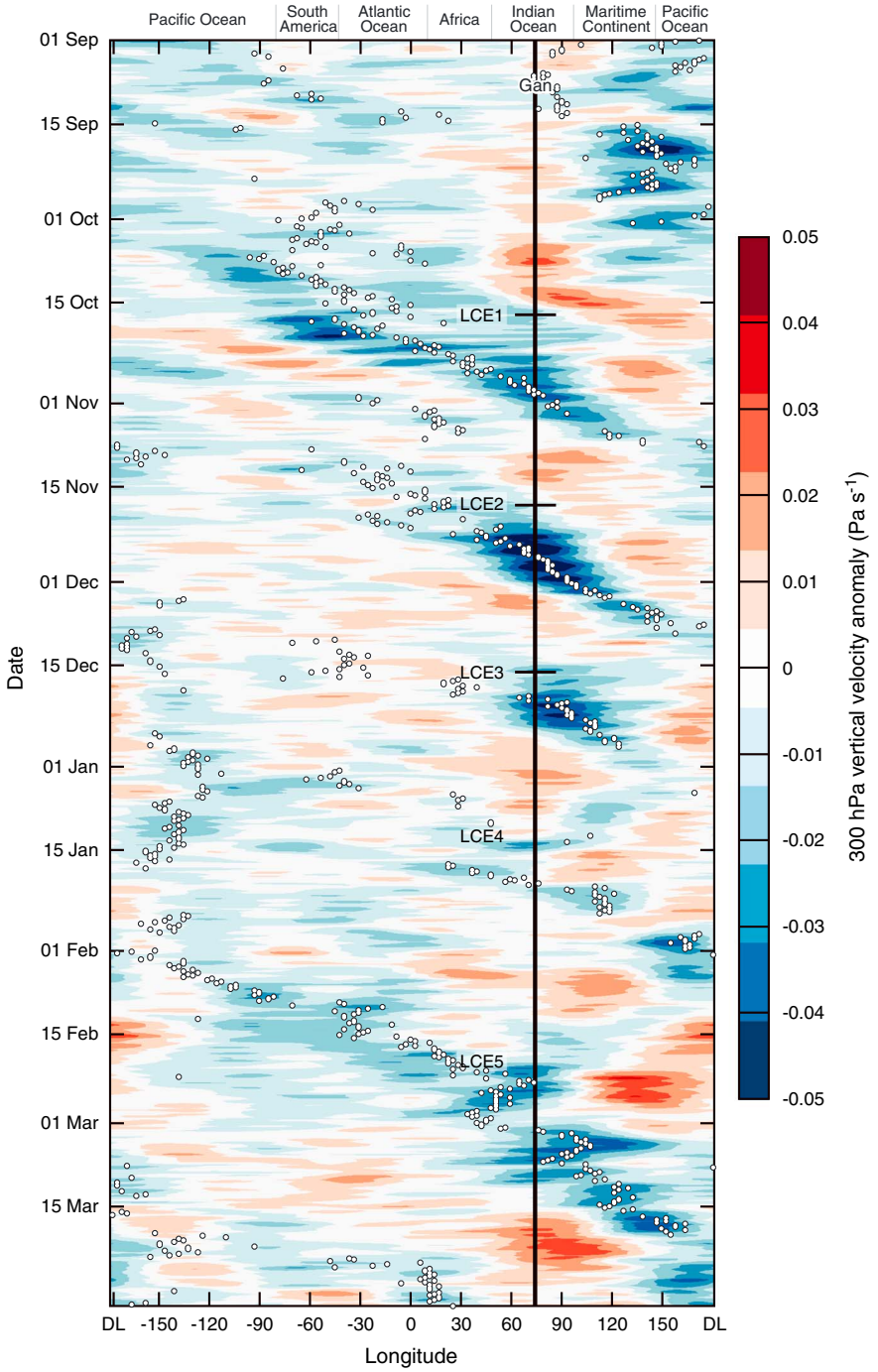

Figure 4. Time-longitude plot of the smoothed 300 hPa ω' field derived from ERA-I averaged between 3°N and 3°S. Smoothing was completed with $\sigma_x = 27$ and $\sigma_y = 13$ as described in the text. The black lines are described in Figure 1. The scattered white dots represent the minimum velocity potential anomaly at each time after the velocity potential fields are also smoothed.

$\sigma_x = 54$ and $\sigma_y = 20$, and when applied to the χ_{150}' field, the resulting field has a median magnitude of 78% of the original field. In other words, about 78% of the total velocity potential anomaly can be explained by components of the divergence with zonal wavenumber 1.5 or lower. The Hovmöller for ω' with the new filter is shown in Figure 5. Circumnavigating areas of large-scale upward motion are more clearly seen; however, they arrived after onset of LCEs 1 and 2 at Gan. Westward propagating areas of upward motion

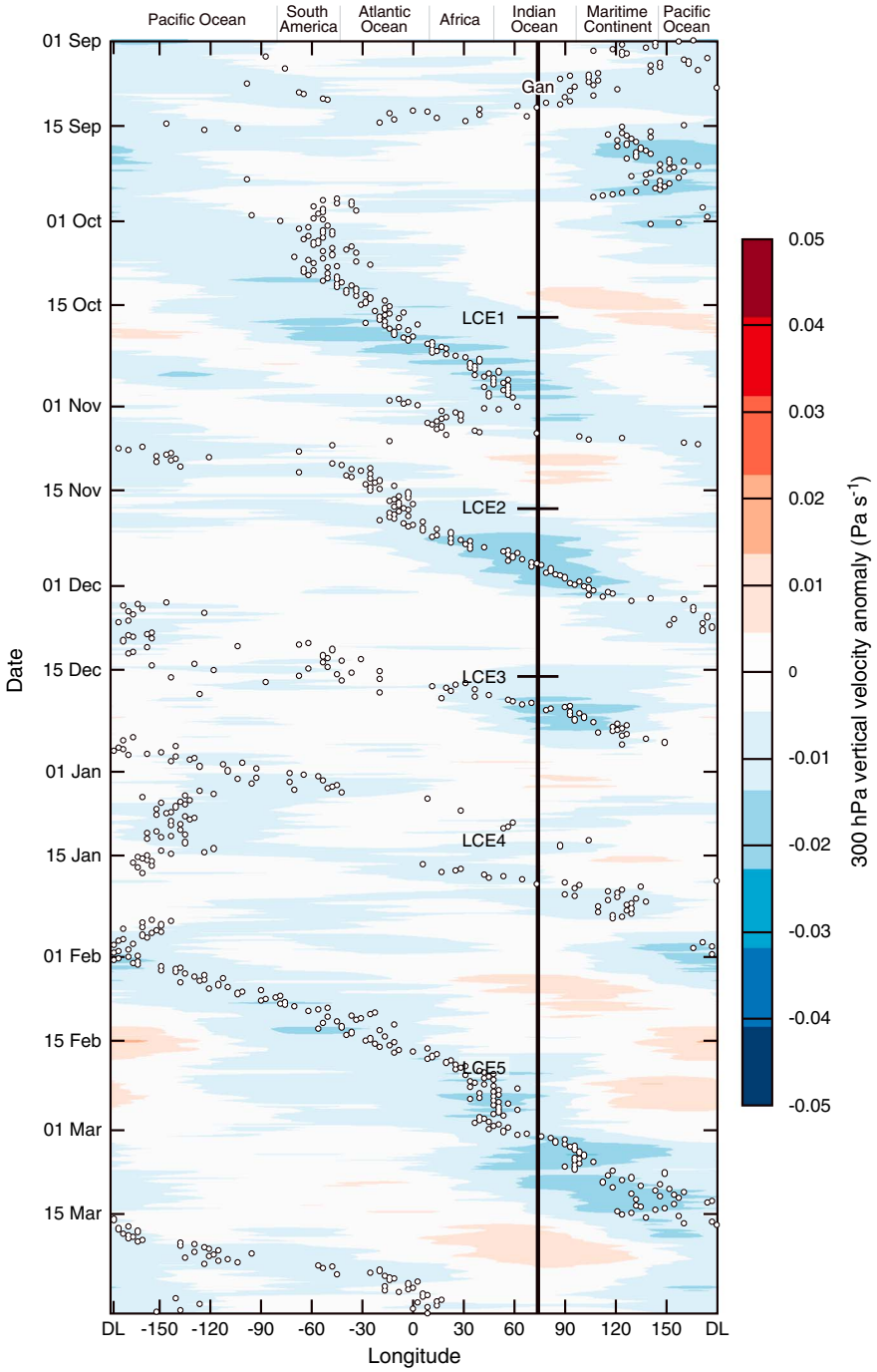

Figure 5. Same as Figure 4 but with $\sigma_x = 54$ and $\sigma_y = 20$.

over the Indian Ocean after LCEs 3 and 4 are not clearly evident. While the components of upper tropospheric vertical motion and velocity potential with lowest zonal frequencies obviously circumnavigated repeatedly, zonally or meridionally narrower features were evidently important for the exact timing of initial convective onset associated with each LCE.

4.2. Longitude-Height Cross Sections of Vertical Velocity and Zonal Wind Anomalies

Figures 6 and 7 show zonal cross sections, respectively, of the filtered vertical velocity and zonal wind anomalies computed with each filter. The gray vectors on each represent the anomalous zonal and vertical velocity using

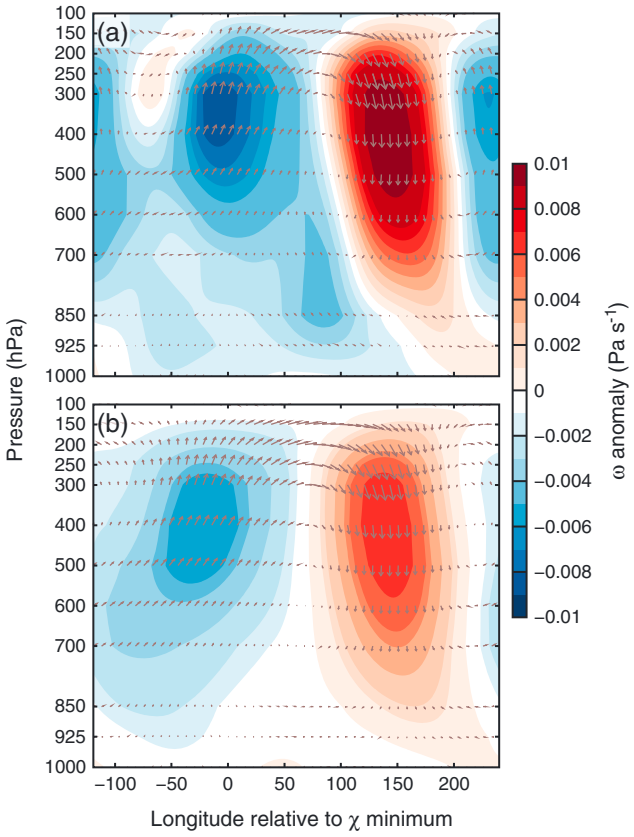

Figure 6. Mean longitude-height cross sections of smoothed ω' derived from ERA-I composited about the longitude of the χ_{150}' minimum as described in the text for (a) $\sigma_x = 27$ and $\sigma_y = 13$ and (b) $\sigma_x = 54$ and $\sigma_y = 20$. The gray vectors represent the anomalous zonal and vertical velocities using each filter, with vertical velocity multiplied by 10^4.

each filter, with vertical velocity multiplied by 10^4. They represent a composite structure of each averaged within 3° of the equator and composited about the longitude at which the 150 hPa velocity potential anomaly with the same smoother applied is a minimum. The composites represent the structures only during periods of suppressed convection and mean large-scale subsidence anomalies over the Indian Ocean, specifically 1–14 October and 10–16 November. Given the small sample size, the signs of vertical motion associated with the ω' structures are not statistically significant except in a few locations where their magnitudes are large. Because equatorial convection was also suppressed during these periods in the Western Hemisphere, the anomalies, with one important exception detailed below, were not strongly influenced by diabatic heating. Figure 6a is the ω' cross section for $\sigma_x = 27$ and $\sigma_y = 13$. The maximum magnitude of ω' was about 0.008 (0.01) Pa s^{-1} in the ascending (descending) branch and occurred between 300 hPa and 500 hPa. The ω' was tilted westward with height so that anomalous subsidence first gave way to anomalous upward motion in the lower troposphere about 150° longitude to the east of the χ_{150}' minimum. Such a tilted structure is consistent with a buildup in the depth of convection over the Indian Ocean as the structure moved eastward and subsidence was reduced. The exception mentioned above to the filtered ω' representing a dry signal is an effect of the small filter passing disturbances of up to wavenumber 3. The lower tropospheric upward motion anomalies east of the minimum in omega at 300–500 hPa are probably associated with shallow convection. The maximum magnitudes for ω' using the larger filter ($\sigma_x = 54$ and $\sigma_y = 20$; Figure 6b) occurred between 300 hPa and 500 hPa and are between 0.005 (0.007) Pa s^{-1} for the ascending (descending) branch. The downward (upward) portion of the ω' structure was tilted westward (eastward) with height. Recall that the structure in Figure 6b preserves wavenumbers 1.5 and lower; the wavenumber 1 structure (not shown) is not tilted with height but the magnitude of its signal is one third to one half of that shown in Figure 6b. The vertical motion is consistent with a completely dry mass continuity response to the zonal wind/divergence structure seen in Figure 7 below.

Regardless of the smoothing used, structures of zonal wind anomalies (u') are very similar (Figure 7), meaning that the zonal wind signal was predominantly wavenumber 1.5 or lower in structure. Westerly (easterly) anomalies were maximized at 150–200 hPa and were tilted eastward with height. The direction of the tilt with height was, interestingly, in contrast to that found within a convectively active MJO region [i.e., *Kiladis et al.*, 2005]. We also checked the composite u' structure during periods of active MJO convection (not shown) and found u' structures that did tilt westward with height as in *Kiladis et al.* [2005]. The ω' seen in Figure 6b is consistent with divergence/convergence patterns throughout the troposphere as seen in Figure 7. The smooth structure of zonal wind anomalies probably determined broadly where anomalous ascent and descent occurred, while higher-frequency disturbances or regional dynamics probably

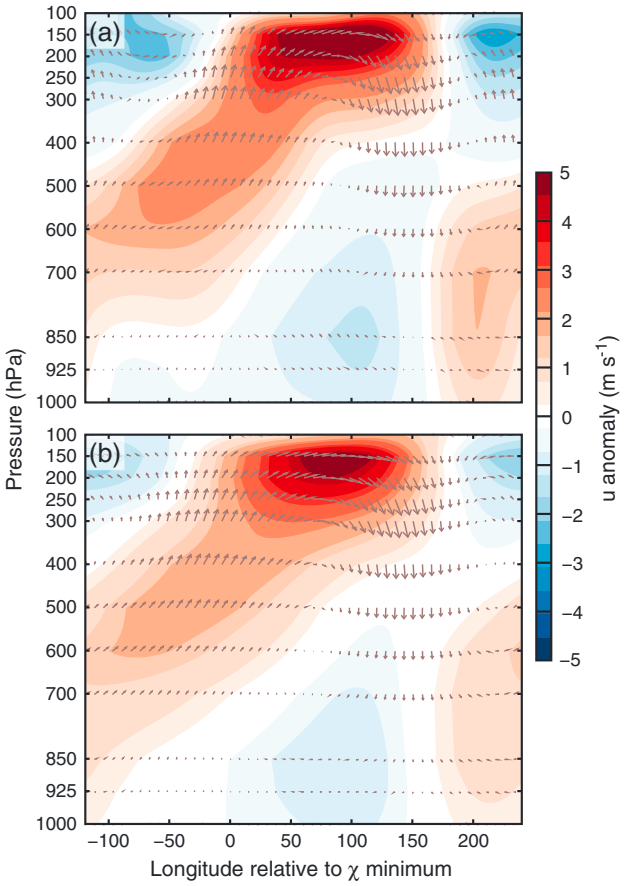

Figure 7. Same as in Figure 6 but for *u*′.

contributed to the tilted structure seen in Figure 6a and may have been more important for determining exactly when MJO convective onset occurred and how quickly convection transitioned from shallow to deep.

5. Large-Scale Conditions Prior to Formation of Medium and Deep Cumulonimbi and Before LCE Onset

5.1. Methodology

Kumar et al. [2014; hereafter K14] concluded that large-scale vertical motion, and the resulting vertical advection of moisture caused by it, was the critical ingredient necessary for formation of widespread deep cumulonimbus clouds near Darwin, Australia. Using a similar methodology, we reach the same conclusion for the convection observed by S-PolKa at Addu City during DYNAMO/AMIE. However, given the time scale involved for MJO onset compared to the time scale involved for individual clouds to grow into deep cumulonimbi, our reasoning and interpretation are somewhat different. Unless stated explicitly, the methods used in this section are the same as those of K14.

In brief, K14 tracked convective cells having a 0 dBZ echo top height (ETH) between 3 and 7 km to determine the mean vector motion of cells within the radar volume of interest. They then searched downstream of the cell to determine the probability of that cell having grown into a deep cumulonimbus (0 dBZ ETH $>$ 9 km). They then studied large-scale conditions in the hours prior to times dominated by cells that grew into deep cumulonimbus (Cb) and prior to times dominated by cells that did not. Large-scale regimes prior to deep Cb periods were preceded by enhanced upward motion, vertical advection of moisture, and relative humidity between 600 and 300 hPa. Lapse rates during the regimes prior to times with deep and medium Cb were, in contrast, very similar. For clarity, we henceforth refer to the 3–7 km cells that we track as $Cb_{3-7\,km}$, and we will use "Cb" and "Cg" to describe the $Cb_{3-7\,km}$ cells after they did or did not deepen, respectively. Cg refers colloquially to precipitating congestus clouds.

K14 use Thunderstorm Identification, Tracking, Analysis, and Nowcasting (TITAN) software [*Dixon and Wiener*, 1993] to track cells. Because we track a large number of stratiform elements as well in order to obtain mean cloud motion, the Tracking Radar Echoes by Correlation package within TITAN is more appropriate [*Dixon*, 2005]. As such, no minimum area or reflectivity requirement is necessary for cell tracking as in K14.

Henceforth, large-scale environmental regimes will be referred to as "Cb regimes" or "Cg regimes." The regimes refer to the environmental conditions or the time period during the 6 h prior to the 6 h block during which the clouds were observed. We refer to the times during which the clouds were observed as "Cb periods" or "Cg periods," such that, for example, Cg regimes occur before their corresponding Cg periods. As in K14, the ratio of Cb to the sum of Cb and Cg within 6 h long time periods (00:00–06:00 UTC, 06:00–12:00 UTC, 12:00–18:00 UTC, and 18:00–00:00 UTC) determined whether each 6 h block was dominated by Cb or Cg. Using the same tercile criteria as K14, any 6 h period in which that ratio was zero followed a Cg regime. Any 6 h period during which the ratio exceeded 0.26 followed a Cb regime. We refer

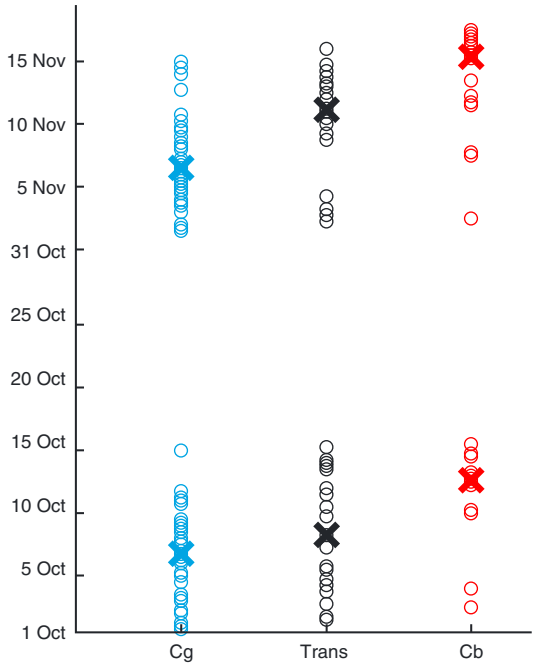

Figure 8. Times and dates of Cg, transition, and Cb periods. The two X symbols in each column represent median times/dates of each period prior to the October and November large-scale convective events.

to periods in which the ratio was >0 but < .26 as "transition periods," which were preceded by "transition regimes." Figure 8 represents the temporal distribution of each period. In Figure 8, each blue, black, or red circle represents a time/date classified as a Cg, transition, or Cb period, respectively. The two "X" marks in each column represent the median times/dates of occurrence of each period prior to the October and November LCEs. The median dates/times are 6 October, 06:00 UTC and 6 November, 00:00 UTC (Cg); 7 October, 18:00 UTC and 10 November, 15:00 UTC (transition); and 12 October, 03:00 UTC and 14 November, 21:00 UTC (Cb).

K14 created the above methodology to study the effect of the large-scale environment on the growth of cumulonimbi on time scales of hours. In contrast, the large-scale evolution of the cloud population prior to MJO onset occurs over days. As seen in Figure 8, the largest density of Cg periods occurs several days prior to MJO onset, and Cb periods occur most commonly closer to MJO onset. What we label as transition periods occur whenever the radar does not see enough Cb to classify the time as a Cb period. This can happen anytime during the evolution of the cloud population. On average, during the two MJO cases included in this study, small but nonzero occurrence of Cb (i.e., a transition period) is maximized after the highest frequency of Cg periods and before the highest frequency of Cb periods. Therefore, the composite large-scale environments prior to MJO convective onset, when compared, depict a transition from a Cg regime to a Cb regime. For consistency with K14, we have chosen to examine the environment 6 h before clouds are observed; however, the changes in the large-scale environment that are of interest to us occur over days. If we examine the environment during the period of observed growth instead of 6 h before it, our results are the same.

Environmental fields demonstrated in this section are derived from rawinsonde data (Figure 9) or large-scale forcing (Figure 10) and are used to characterize conditions during each regime. All results in these figures are composited over all times/dates during which a Cg, transition, or Cb regime is present. For large-scale forcing, variables are averaged within an area bound by 3°S, 3°N, 71°E, and 76°E, the approximate bounds on the entire S-PolKa surveillance domain.

5.2. Results

A total of 10,325 $Cb_{3-7\,km}$ cells were identified. Of those, 2725 had at least 80% likelihood of growing into a Cb. The 1:2.8 ratio between Cg and Cb is identical to that reported by K14. Because we are interested in large-scale conditions prior to MJO convective onset, we will only investigate Cb and Cg environments during convectively suppressed periods prior to LCE onset, or from 1 to 15 October and 1 to 17 November. Within these periods, 986 Cb cells developed during Cb periods, and 2003 Cg cells were observed during Cg periods.

Figure 9 shows profiles of relative humidity (RH), lapse rate, temperature, and specific humidity characteristic of Cg and Cb environmental regimes. All profiles are derived from the Gan rawinsonde data. Shaded regions cover the 95% confidence interval for each field, except for in Figure 9c, in which the intervals are approximately the widths of each line. The 95% confidence intervals are computed using the bootstrapping technique used in K14 and described in greater detail by *Chu and Wang* [1997]. As in K14, no consistent or significant difference is noted in the lapse rates between the two environmental regimes at any height (Figure 9a). In fact, in the upper half of the troposphere, the lapse rates approached the climatological moist adiabat as in *Mapes* [2001]. The static stability prior to Cb development was not greater than it was prior to periods during which Cb were not prevalent. The RH profile (Figure 9b) during

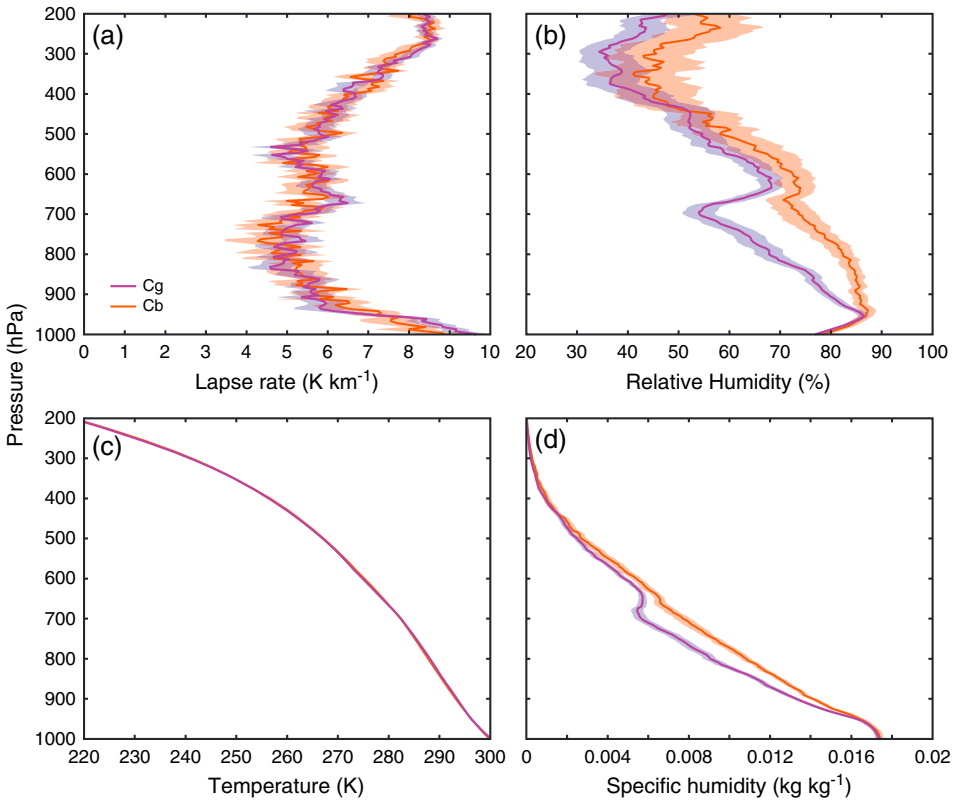

Figure 9. Vertical mean profiles derived from Gan rawinsonde data of (a) lapse rate, (b) relative humidity, (c) temperature, and (d) specific humidity during Cg (purple) and Cb (red) environmental regimes. The shaded region of corresponding color covers the 95% confidence interval of each mean.

the Cb regime was 10 to 15% (absolute RH%) greater between 900 and 650 hPa, while the RH profile above 600 hPa was fairly consistent between regimes, especially considering the low absolute humidity present aloft. Figures 9c and 9d are shown to illustrate that RH was largely controlled by specific humidity. The temperature difference between regimes at all levels was < 1 K. The low RH (50–60%) near 700 hPa during the Cg regime was probably related to a climatological minimum in cloudiness and humidity near that level in the tropics [*Zuidema*, 1998; *Yoneyama*, 2003]. Greater low tropospheric humidity during Cb regimes was likely responsible for the growth of $Cb_{3-7\,km}$ clouds (section 1). Table 1 shows the 95% confidence range for the number Cg or Cb occurring during Cg, transition, or Cb regimes. Essentially the same number of Cg was present during Cg regimes as during Cb regimes, but the number of Cg was larger during transition regimes. Thus, the differences in tropospheric RH during the Cg and Cb regimes might be explained by the potentially larger number of Cg cells during transition regimes, but the mere presence of a large population of Cg elements does not mean that convection deepened.

Figure 10 displays profiles of vertical velocity (omega), apparent heat source (Q_1), apparent moisture sink (Q_2), horizontal moisture advection (HADV), vertical moisture advection (VADV), total moisture advection (TADV = HADV + VADV), and Eulerian moisture tendency ($\partial q/\partial t$) derived from large-scale forcing during Cg (purple), transition (black), and Cb (red) regimes. The 95% confidence interval for each profile is calculated as above and is shown as a shaded region. The median of the distribution of means obtained by the bootstrapping method is shown as a solid line within the shaded region, and our discussion below will focus on relationships between these means. Because of the small sample size used, many of our statements or conclusions below cannot be proven to be statistically robust. However, a comparison of the mean profiles is nonetheless interesting, and the following results are broadly consistent with those of *Ruppert and Johnson* [2015]. Upward motion (Figure 10a) increased slightly between Cg and transition regimes, while Q_1 (Figure 10b) remained similar but was generally slightly larger during transition regimes. Greater upward motion and heating during Cb regimes was certainly a consequence of the fact that a large amount of deep convection

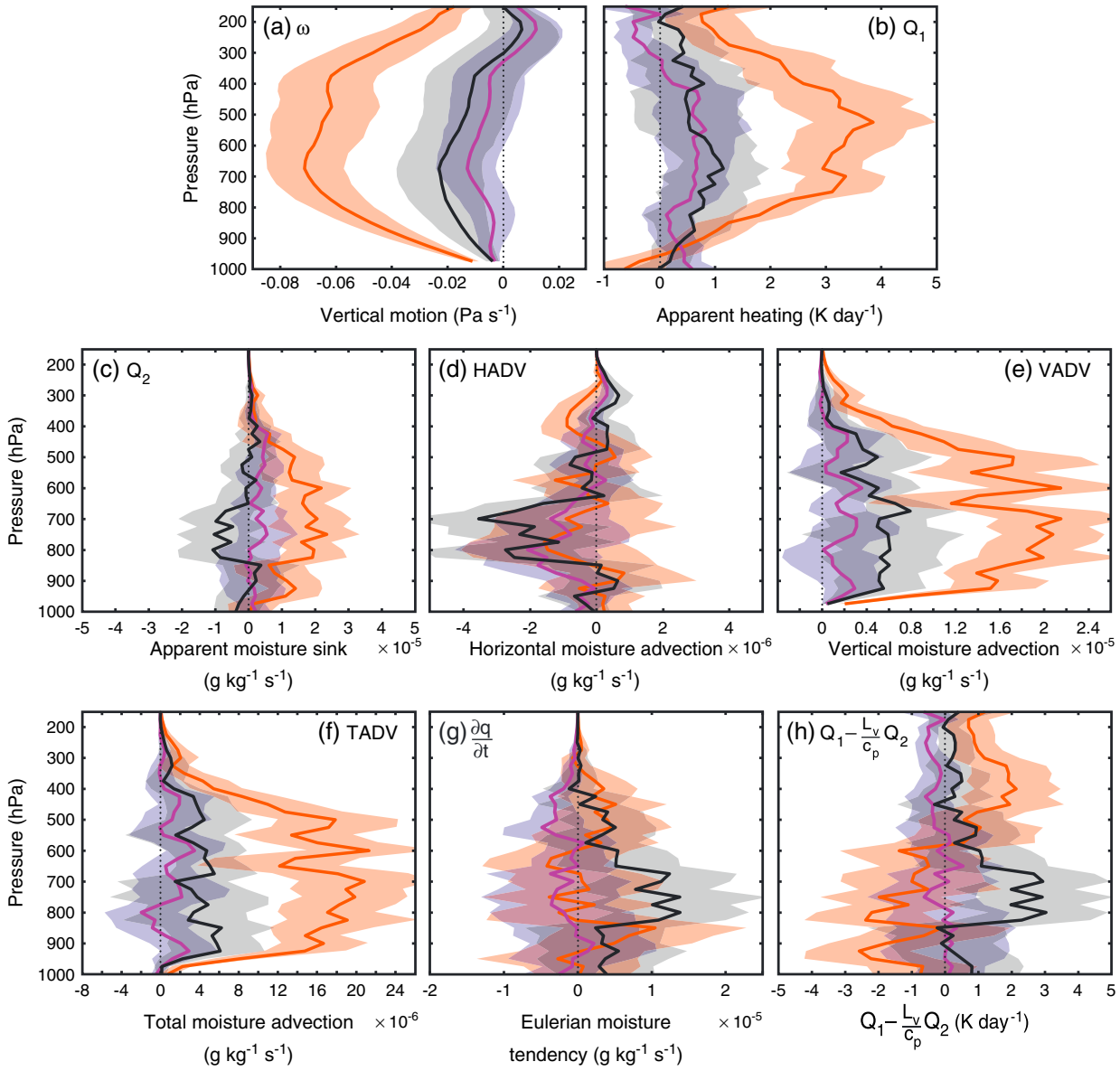

Figure 10. Vertical profiles of (a) vertical velocity (ω), (b) apparent heating (Q_1), (c) apparent moisture sink (Q_2), (d) horizontal moisture advection, (e) vertical moisture advection, (f) total moisture advection, (g) Eulerian moisture tendency, and (h) $Q_1 - L_v Q_2/c_p$ derived from a large-scale forcing data set as described in the text. The purple, black, and red lines represent the estimated mean at each level during Cg, transition, and Cb environmental regimes, respectively. The shaded region of corresponding color covers the 95% confidence interval of each mean. All fields are averaged between 3°N, 3°S, 71°E, and 76°E.

was already present (Table 1). Q_2 (Figure 10c) was near zero throughout the troposphere during Cg regimes, negative (meaning moistening) between 850 and 650 hPa during transition regimes, and positive through a deep layer during Cb regimes. Similar wide ranges of drying by horizontal advection (HADV) were seen during all regimes (Figure 10d). Vertical moisture advection (VADV) was small but positive above 400 hPa during Cg regimes and 2–3 times larger during transition regimes. However, VADV approached zero above 400 hPa during transition regimes as well, consistent with the small number of Cb observed in the following 6 h period (Table 1). VADV was large throughout the

Table 1. The 95% Confidence Range of the Number of Cg or Cb Present During Cg, Transition, and Cb Environmental Regimes As Described in the Text

Cloud Type/Regime	Cg Regime	Transition	Cb Regime
Cg	26–43	37–69	19–44
Cb	0	5–10	24–63

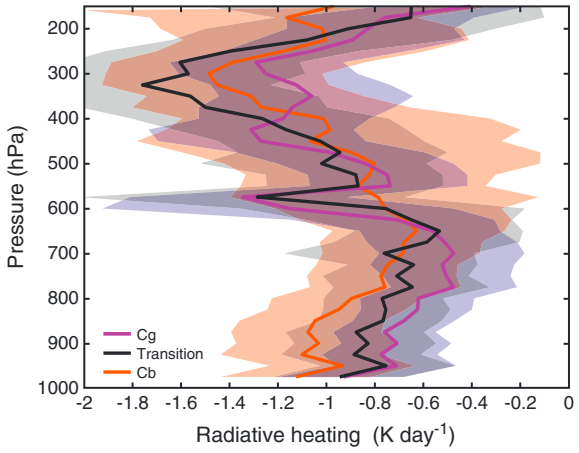

Figure 11. Mean total radiative heating (longwave + shortwave) rates during Cg (purple), transition (black), and Cb (red) regimes. The shaded region of corresponding color covers the 95% confidence interval of each mean.

troposphere during Cb regimes. The resulting total moisture advection (TADV) is shown in Figure 10f.

The Eulerian moisture tendency $\partial q/\partial t$ is

$$\frac{\partial q}{\partial t} = -\mathbf{v}_h \cdot \nabla q - \omega \frac{\partial q}{\partial p} - Q_2, \tag{1}$$

in which v_h is the horizontal wind vector and q is the specific humidity. The profiles of $\partial q/\partial t$ are shown in Figure 10g, which shows three interesting features: drying above 500 hPa during Cg regimes, relatively rapid moistening between 850 hPa and 600 hPa during transition regimes, and moistening between 550 and 350 hPa during Cb regimes. Q_2 in the large-scale forcing data set was computed using the other three terms in equation (1) and can be defined ignoring ice processes following *Yanai et al.* [1973] as

$$Q_2 = (\overline{c} - \overline{e}) + \frac{\partial}{\partial p}\left(\overline{\omega' q'}\right), \tag{2}$$

in which c and e, respectively, represent condensation and evaporation rates. The overbars represent means within a fraction of the large-scale domain of interest large enough to contain a representative sample of the large-scale cloud population. Primes represent deviations from that mean and represent subgrid scale processes occurring above the surface within convective updrafts that are not resolved even at "cloud-resolving" (e.g., order of 1 km) horizontal resolution. The final term in equation (2) represents the vertical eddy flux divergence of eddy moisture, which above the surface, represents cloud moistening via vertical mass transport. The moistening necessary to achieve the RH profile (Figure 9a) during Cb regimes occurred during transition regimes (Figures 10c and 10g). An increased number of Cg elements was seen in the lower troposphere during brief transition regimes (Table 1). This certainly increased vertical eddy flux divergence of moisture and possibly evaporation of cloud condensate into the environment via detrainment from middle and upper portions of Cg. However, we cannot definitively tell from our current observational data set whether either term in equation (2) is mostly responsible for positive moisture tendencies in equation (1) or their contributions are similar. However, consider the equation for Q_1 ignoring ice processes [*Yanai et al.*, 1973]

$$Q_1 = Q_R + \frac{1}{c_p}\left[L_v(\overline{c} - \overline{e}) - \frac{\partial}{\partial p}\left(\overline{\omega' s'}\right)\right], \tag{3}$$

in which c_p is the specific heat of water at constant pressure, Q_R is the radiative heating, L_v is the latent heat of vaporization, s is the dry static energy, and overbars and primes are as in equation (2). The Q_1 profiles during transition regimes were very similar to those during Cg regimes. Multiplying equation (2) by L_v/c_p then subtracting equation (2) from equation (3) yields

$$Q_1 - \frac{L_v}{c_p} Q_2 = Q_R - \frac{1}{c_p}\frac{\partial}{\partial p}\left(\overline{\omega' h'}\right). \tag{4}$$

in which $h = s + L_v q$ is the moist static energy (MSE). The values of equation (4) are shown in Figure 10h, although the plotted values include ice processes where applicable. We are, however, interested in its value in the lower troposphere. During Cg regimes, equation (4) yields $Q_1 - L_v Q_2/c_p \approx 0$ at all levels, meaning that the vertical flux divergence of MSE approximately balanced cooling by radiation. During transition regimes, $Q_1 - L_v Q_2/c_p$ was distinctly positive between 850 and 650 hPa, but the relative contributions of heat and moisture flux divergences are unknown. The mean radiative (longwave + shortwave) cooling rates as derived by *Feng et al.* [2014] are no more than 0.2 K d^{-1} more during transition regimes than during Cg regimes (Figure 11) and so do not contribute significantly to changes in equation (4) between regimes. It is also interesting to note the peak in

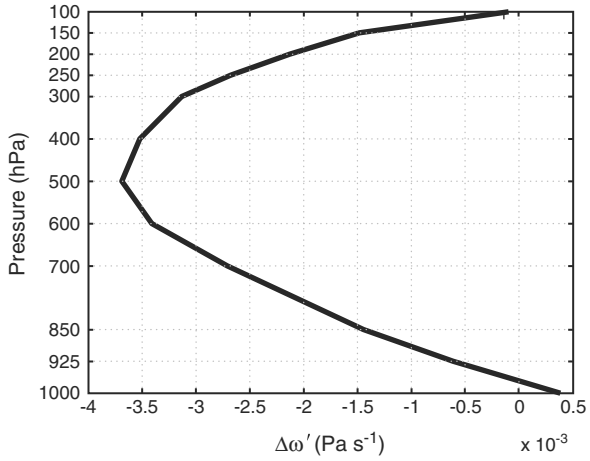

Figure 12. Difference in large-scale ω' ($\sigma_x = 54$ and $\sigma_y = 20$) between transition and Cg periods using the method described in the text.

longwave cooling between 550 and 650 hPa during Cg and transition regimes. This likely represents infrared cooling from the tops of congestus clouds. The altitude of the cooling is consistent with the top of the layer in which $Q_1 - L_v Q_2/c_p$ is distinctly positive.

A modeling study that resolves convective processes will be necessary to estimate the relative contributions of sensible and latent heat flux divergence to the eddy MSE flux divergence, but either potential moistening process (evaporation and eddy flux divergence of moisture) is likely related to moist convection. However, congestus clouds were also present during Cg periods and did not cause moistening. Why did they become more numerous and begin moistening the lower troposphere?

6. Connecting Large-Scale Anomalous Vertical Motions and Cloud Moistening

As the large-scale zonal wind anomaly (Figure 7) propagated eastward around the globe, a wavenumber 1 vertical velocity anomaly (Figure 6b) moved with it. During a convectively suppressed period over the Indian Ocean, large-scale subsidence associated with this feature eventually decreased through much of the troposphere. From a budgetary point of view, and assuming minimal changes in temperature in accordance with Figure 9c, a reduction in adiabatic cooling associated with a reduction in mean large-scale subsidence must be balanced by a reduction in radiative cooling or an increase in convective heating to maintain radiative convective balance. Figure 12 shows the difference in ω' at Gan (73.15°E) between the median times/dates of transition regimes and Cg regimes (Figure 8). We compute this difference by first determining the average longitude of the χ_{150}' minimum (smoothed here with the large filter for consistency) during the times/dates within 12 h of the median ones mentioned in section 5.1. The Cg and transition median dates are separated by an average of 4 days. During Cg (transition) regimes, Gan was an average of 126° (84°) longitude east of the χ_{150}' minimum. The representative ω' profile for each regime is then taken from the appropriate longitude (to the right of the zero reference longitude) in Figure 6b.

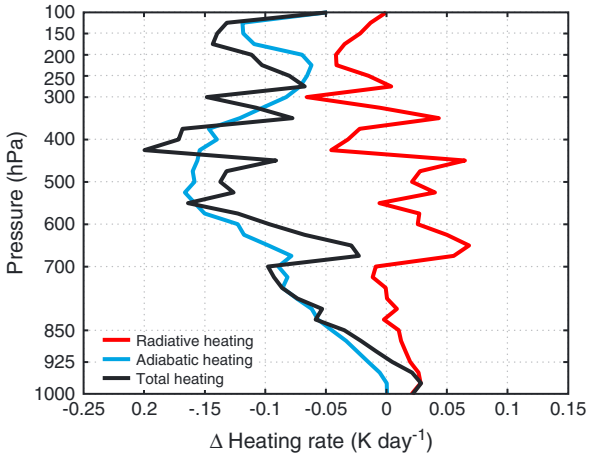

Figure 13. Changes in adiabatic (blue) and radiative (red) heating rates directly associated with the difference in ω' shown in Figure 12. The black line is the sum of the red and blue lines.

The blue line in Figure 13 depicts the change in adiabatic heating rate associated with the reduction in subsidence illustrated in Figure 12. We then, assuming that a constant vertical motion of half was seen in Figure 12, determine a new humidity profile associated directly (i.e., with no moist convection) with vertical advection of moisture under the reduced subsidence for a period of 4 days. We are then able to compare two vertical profiles of humidity—one each for the Cg regime, taken from Figure 9d, and the transition regime, derived using the one in Figure 9d and the vertical motion in Figure 12. Using pressure levels spaced by 25 hPa and ranging from 100 to 1000 hPa, the temperature profile associated with the Cg regime, a constant sea surface temperature of 302 K, and standard profiles of atmospheric trace gases (CO_2, O_3, N_2O, CO, CH_4, and O_2) included in the Rapid

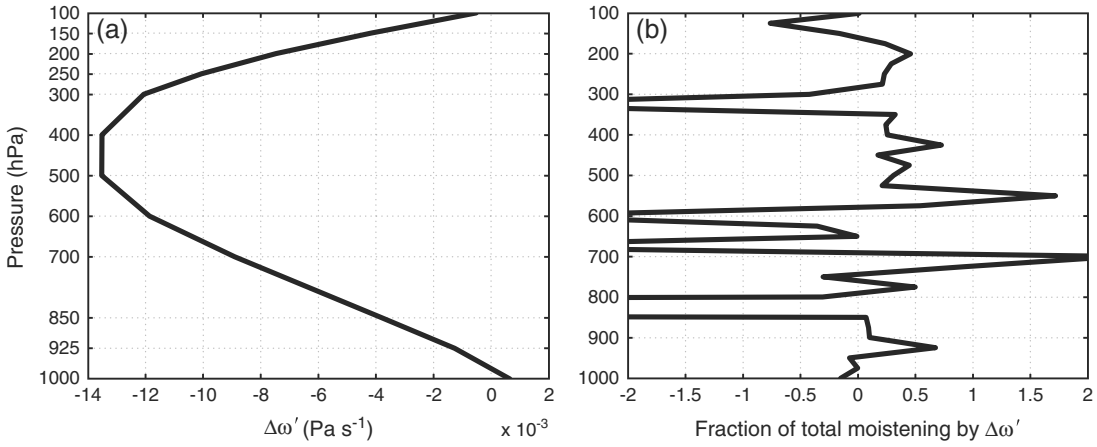

Figure 14. (a) As in Figure 12 but for ω' difference between Cb and Cg periods using $\sigma_x = 27$ and $\sigma_y = 13$. (b) Fraction of total positive moistening during Cb periods attributed to the change in vertical motion shown in Figure 14a.

Radiative Transfer Model (RRTM) [*Mlawer et al.*, 1997], we insert each of the humidity profiles into RRTM and examine the aggregate change in longwave radiative heating rates assuming the change in water vapor detailed above occurred instantaneously. The red line in Figure 13 depicts the change in radiative heating rate, and the black line is the sum of the changes in adiabatic and radiative heating rates. If the two balanced, the black line would follow 0. Except below 925 hPa, the increase in radiative heating by water vapor was insufficient to balance the reduced adiabatic heating caused by a reduction in subsidence. Near the surface, vertical motion approaches zero, and so the increase in radiative heating dominated the total change in heating rate. Between 700 and 925 hPa, reduction in adiabatic heating dominated the change in heating rate. Thus, the reduction in subsidence acted to steepen the lapse rate below 700 hPa. Integrating the changes in heating seen in Figure 13 over 4 days, the reduction in subsidence acted to steepen the 1000–700 hPa lapse rate by about 0.16 K km^{-1}. Even if we do not assume that moistening occurred instantaneously, the reduction in adiabatic heating alone is enough to force some lapse rate steepening below 500 hPa. The slight destabilization of the environment was favorable for development of more congestus-like convection, which in turn acted to help balance the deficit in heating and probably to restore the lapse rate so that it did not change significantly between Cg and Cb regimes (i.e., Figure 9a). The moderately deep convection moistened the lower troposphere as discussed in section 5 and then deep convection developed. Under strong subsidence, moderately deep (and even 15 km or deeper) cumulonimbi can still exist, but they apparently cannot efficiently moisten the troposphere.

Another interesting feature is the moistening of the upper troposphere during Cb regimes. Figure 14a is a plot similar to Figure 12 except for a difference between Cb regimes and Cg regimes using the ω' for the smaller filter (Figure 6a). Here we use ω' from the smaller filter because we are interested in dry large-scale vertical motions in the upper troposphere even if they are not wavenumber 1 structures. We then, assuming all else equal, find that the increase in VADV associated with the change in ω' accounted for 15–25% of the difference in $\partial q/\partial t$ at 300–500 hPa between Cb and Cg regimes (not shown). Figure 14b shows a profile of the fraction of the total positive moistening during Cb regimes (Figure 10g) that can be explained by the increase in VADV associated only with the change in ω' seen in Figure 14a. At most levels $\partial q/\partial t$ was small during Cb regimes and the plot in Figure 14b probably means little, but between 525 and 350 hPa, where $\partial q/\partial t$ was distinctly positive, changes in ω' contributed to ~25–50% of the total moistening occurring during Cb periods. Thus, while deep convection could moisten the upper troposphere independently, the portion of the large-scale ω anomaly aloft that was not directly caused by the deep convection expedited the process, more rapidly making the large-scale environment favorable for stratiform regions of precipitation to develop.

7. Conclusions

We have explored the propagation of anomalies of velocity potential and vertical motion into the Indian Ocean region during the DYNAMO/AMIE field campaign (October 2011–March 2012). *Powell and Houze* [2013] (PH13) documented periodicity of ~30 days in upper tropospheric zonal wind above 300 hPa and

temperature and humidity anomalies between 200 and 500 hPa over and near Gan Island, which is located in the central equatorial Indian Ocean in the region where MJO-related convection was seen to occur first for three individual large-scale convective events (LCEs) observed by radar. The frequent vertical profiles of tropospheric, dynamic, and thermodynamic structure provided by rawinsonde data at Gan, however, do not provide any information about the evolution of such anomalies as they moved through the tropics. Nor do they tell whether the anomalies were directly caused by the anomalous convection over the Indian Ocean, existed prior to convective development and propagated into the region of convective onset, or, in the latter case, played a role in facilitating the convection.

Global reanalysis fields, however, show that velocity potential (χ) anomalies at 150 hPa propagated into the Indian Ocean from the west and that these anomalies were dominated by anomalies in zonal wind [*Gottschalck et al*., 2013; *Powell and Houze*, 2013]. Negative anomalies of χ may have circumnavigated continuously during the period studied, thus indicating the possibility that all of the LCEs examined were successive MJO events (in the manner suggested by *Matthews* [2008]). For the cases during which ground-based radar data were obtained, the negative χ anomaly arrived 0–2 days prior to observation of the first MCS near Gan. The negative anomaly also arrived over the Indian Ocean in January, suggesting that the area of precipitation then observed south of the equator [*Yoneyama et al*., 2013] and outside of our analysis domain may have been linked to similar dynamics that forced previous LCEs.

Large-scale vertical motion fields in the tropics have been obtained by applying a spatial Gaussian smoother to the vertical velocity field from reanalysis. We obtain a large-scale structure that is consistent with most of the total velocity potential anomaly and one that appears to circumnavigate the globe several times. The wavenumber 1 150 hPa velocity potential anomaly is consistent with a mass continuity response to wavenumber 1 patterns of upper tropospheric divergence and lower tropospheric convergence given boundary conditions of zero vertical motion at the surface and the tropopause. The anomalous vertical motions even persisted over the Western Hemisphere, where widespread precipitation (and thus deep latent heating) was not usually present near the equator. Higher wavenumber westward propagating anomalies of large-scale vertical motion sometimes also originated over the Maritime Continent and west Pacific and moved over the Indian Ocean. Negative velocity potential at 150 hPa and large-scale upward motion anomalies at 300 hPa reached the longitude of Gan 0–2 days prior to onset of three LCEs observed by radar.

We have closely followed the approach of *Kumar et al*. [2014] to determine large-scale conditions present during periods in which moderately deep (3–7 km) cumulonimbi predominantly grew into deep (>9 km) cumulonimbi (Cb regime) and during periods in which they mostly did not (Cg regime) and periods during which some clouds developed into deep cumulonimbi but not frequently enough to be classified as a Cb regime (transition regime). We show that static stability in the troposphere was the same during Cb and Cg regimes but that relative humidity was 10–15% greater below 600 hPa during Cb regimes. Thus, deep convection was sensitive to low tropospheric humidity. Gradual changes in large-scale tropospheric static stability do not appear to play a major role in enhancing or suppressing convection in relation to MJO convective onset. Instead, the larger RH during Cb regimes was likely related to an enhanced number of congestus elements during transition regimes. We conclude that the ability of moderately deep clouds to grow unrestrictedly into deep cumulonimbi was related to large-scale vertical motions via low-tropospheric moistening by these additional congestus. The clouds moistened the environment via evaporation and/or vertical flux convergence of moisture. A reduction in subsidence through a deep layer ahead of an upper-level velocity potential minimum acted to steepen the lapse rate in the lower troposphere (Figure 13), promoting more moist convection. The resulting deep convection moistened the upper troposphere and that moistening was reinforced by an increase in large-scale upward motion associated with the dry MJO signal (Figures 6, 7, and 14) as it advanced eastward into the Indian Ocean. The moistening accomplished by both allowed for deep convection to expand laterally into mesoscale systems with large stratiform regions within about 2 days. These resulting expansive stratiform regions are characteristic of MJO convection [*Barnes and Houze*, 2013; *Powell and Houze*, 2013; *Yuan and Houze*, 2013], and they contribute, perhaps largely, to latent heating through a deep layer, especially at upper levels, facilitating "top heavy" heating profiles.

The above findings are consistent with several prior studies that have investigated the relationship between large-scale motions and deep convection. They illuminate how zonal wind anomalies, which are largest and

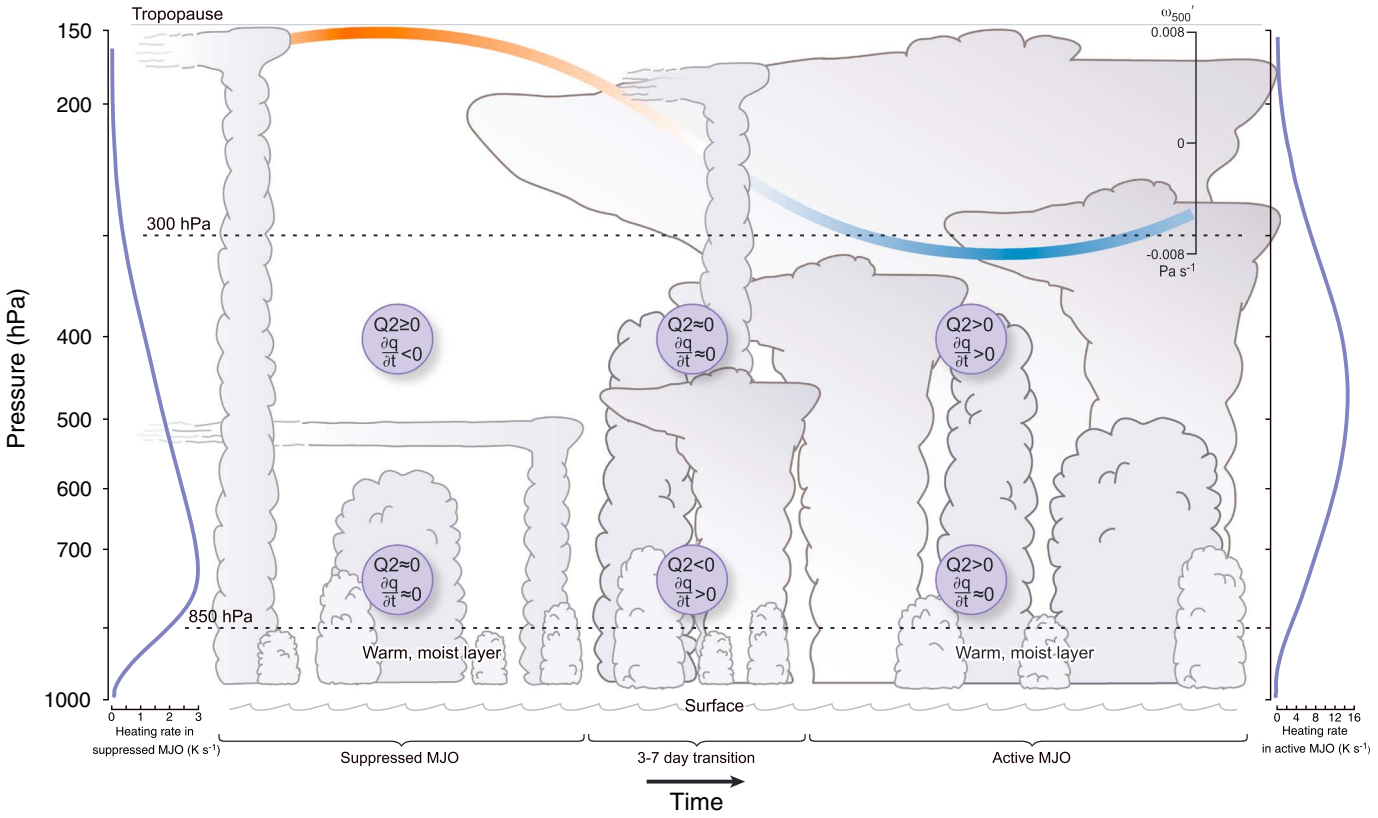

Figure 15. Diagram of moisture tendency, Q_2, and large-scale vertical motion superimposed on the cloud population observed during the periods leading up to MJO convective onset during DYNAMO. Q_2 and Eulerian water vapor tendency are indicated within purple circles for the lower and upper troposphere during suppressed, transition, and active periods. Large anvil clouds reaching near 300 hPa and above represent broad stratiform regions with embedded convection. Smaller clouds represent the presence of congestus mode clouds, medium cumulonimbus, and shallow precipitating clouds of various depths and widths. The red, white, and blue curve represents an approximation of anomalous large-scale vertical motion at 500 hPa associated with an eastward propagating wavenumber 1 circumnavigating feature, and its axis is found top right. The red (blue) indicates anomalous subsidence (upward motion). The blue curves on the left (right) of the figure represent latent heating profiles associated with the convective population during convectively suppressed (active) periods as estimated by the method described in the text.

most easily detected in the upper troposphere, may influence periods of enhanced convection that occurred about 30 days apart during DYNAMO/AMIE. Our efforts are not the first to attempt to relate upper tropospheric dynamics or thermodynamics to MJO convective development. Many prior studies as early as the 1980s (section 1) have suspected such a connection. Some studies have suggested that a Kelvin wave excited by one MJO event can circumnavigate in the upper troposphere and excite the next MJO [e.g., *Seo and Kim*, 2003; *Haertel et al*., 2014], but no physical mechanism through which the Kelvin wave might excite convection has until now been provided. At least partially because of the low sample size used in this study (just two MJO cases), however, most of our results cannot yet be backed by statistical significance of at least 95% (Figures 6 and 7, 9 and 10, and 12–14). Such does not invalidate our results, but it means that uncertainty remains in our conclusions. The results we gain from our limited data set nonetheless yield interesting insight about a plausible relationship between large-scale motions and MJO convective onset.

Figure 15 summarizes the relationship between large-scale vertical motion anomalies and convection preceding and during an active MJO as inferred from our analysis. The conceptual diagram illustrates our interpretation of how convection responds to the large-scale vertical motion associated with the eastward propagating low zonal wavenumber zonal wind structure. The latent heating profile on the left (right) of the figure is computed following *Schumacher et al*. [2004] using typical convective to stratiform rain ratios observed by *Powell and Houze* [2013] during suppressed (active) periods. The apparent moisture sink, Q_2, and the Eulerian water vapor tendency are indicated within purple circles during suppressed, transition, and active periods in the lower troposphere (~600–850 hPa) and upper troposphere (~300–500 hPa). The red, white, and blue curves are a simplified representation of the anomalous large-scale vertical motion at

500 hPa. The convective population is mostly suppressed when the large-scale anomalous vertical motion is downward (red color on curve), and drying occurs throughout most of the troposphere. As the large-scale anomalous subsidence lessens (light color on curve), more deep convection begins to develop and the lower troposphere moistens over 3–7 days [*Powell and Houze*, 2013, 2015]. Q_2 is negative during the moistening, meaning that moistening occurs via eddy convergence of moisture within congestus clouds and/or by detrainment and subsequent evaporation of cloud condensate. Large stratiform regions develop from deep convection and produce deep latent heating profiles during periods of large-scale upward motion (blue color on curve). Moistening of the upper troposphere occurs, although Q_2 is near zero. This requires that large-scale vertical advection of moisture, of which 50–75% is attributed to vertical motions within deep convection, moistens the troposphere above 500 hPa during active periods. The relative numbers of shallow, moderately deep, and deep clouds, as well as their widths during each period, are consistent with observations documented by *Barnes and Houze* [2013] and *Powell and Houze* [2013]; however, the relative sizes of the different types of cloud icons shown in Figure 15 should not be interpreted literally. Real stratiform regions are generally much larger laterally than any individual convective cores observed.

Additionally, we speculate that a mechanism similar to that summarized in Figure 15 may be involved in enhancing or reducing the likelihood of tropical cyclone genesis on intraseasonal time scales throughout the tropics. Relationships between the MJO or velocity potential anomalies and number of tropical cyclones in various basins have been observed [e.g., *Maloney and Hartmann*, 2000a, 2000b; *Klotzbach*, 2010; *Sears*, 2011; *Ventrice et al*., 2013; *Klotzbach*, 2014]. One additional open question involves whether the magnitudes of vertical motion associated with the dry structure illustrated in Figure 6 are actually large enough to cause moistening on the time scales that we observed. Other factors may be important as well. Another concerns why deep convection only sometimes develops when the lower troposphere is sufficiently moist. As of this writing, the authors are conducting a regional modeling study that will attempt to quantify moistening caused by each term seen in equations (2) and (3). We anticipate that the study will also quantify the moisture deposited into the upper troposphere by deep convection and help to clarify the role of divergence anomalies aloft in formation of large-scale convective events of the MJO.

Our conclusions should not necessarily be generalized to all MJO cases, but rather they represent cases that occurred during DYNAMO/AMIE. Environmental conditions need to be favorable through a deep column to support development of mesoscale convective systems. Not all MJO cases are preceded by such an obvious upper-tropospheric velocity potential signal as that shown in this article. In such cases, the mechanism explained herein may not be responsible for exciting a large-scale convective event associated with an MJO. However, for any MJO outbreak to occur, something must make the large-scale environment favorable for deep, widespread convection to spur MJO convective onset, and the mechanism described herein is one such way this may occur.

Appendix A: Smoothing Velocity Potential, Vertical Velocity, and Zonal Wind

To isolate the large-scale divergence and vertical velocity, we apply a Gaussian filter at each data point in the two fields. The window for the filter is 240 data points wide longitudinally by 60 points wide latitudinally, corresponding to 180° of longitude by 45° of latitude. A filter f is applied to each discrete grid point, which we locate at $(x, y) = (0, 0)$, with each model grid point corresponding to one unit in $\boldsymbol{x}$ or $\boldsymbol{y}$ such that

$$f(x,y) = \frac{g(x,y)}{\sum_{x\in[-120,\,120]}\sum_{y\in[-30,\,30]} g(x,y)} \tag{A1}$$

where

$$g(x,y) = \frac{e^{-\left(\frac{x^2}{\sigma_x^2}+\frac{y^2}{\sigma_y^2}\right)}}{2\pi\sigma_x\sigma_y} \tag{A2}$$

In equation (A2), σ_x and σ_y control the flatness of g zonally and meridionally. The σ_x and σ_y are chosen such that they suppress the high-frequency component of the unsmoothed field. Suppose we suppress all signals

with zonal half wavelength less than 60° and meridional half wavelength less than 30° by 90%. To do so, consider that g is constructed of the product of two Gaussians: one in $\boldsymbol{x}$ and one in $\boldsymbol{y}$. For example,

$$g(x) = \frac{e^{\frac{-x^2}{2\sigma_x^2}}}{\sqrt{2\pi}\sigma_x}$$

Its Fourier transform, $G(k)$, in frequency space is

$$G(k) = \frac{1}{\sqrt{2\pi}} e^{\frac{-\sigma_x^2 k^2}{2}} \tag{A3}$$

To suppress all signals with wavelengths less than L by 10%, one can straightforwardly determine σ_x to be

$$\sigma_x = \frac{\sqrt{-2\ln(0.1)}}{2k}, \quad k = \frac{2\pi}{L} \tag{A4}$$

The same exercise may be carried out meridionally, and for the wavelengths described above, $\sigma_x = 27$ and $\sigma_y = 13$. The filtered field f is obtained by taking the matrix sum of the dot product of the filter and the corresponding points in the unfiltered field within the filter window immediately after the seasonal cycle is removed. The denominator in f is only included to normalize the function so that its sum is equal to 1.

Acknowledgments

Beth Tully refined the graphics. The authors were supported by grant DE-SC0008452 from the U.S. Department of Energy and National Science Foundation grants AGS-1059611 and AGS-1355567. C. Zhang, as editor, and six reviewers provided numerous constructive comments and suggestions. The data described in section 2 could be obtained from the following sources at the time of writing: TRMM: http://mirador.gsfc.nasa.gov/cgi-bin/mirador/presentNavigation.pl?tree=project&project=TRMM&dataGroup=Orbital&CGISESSID=1e6fc9c059167aa2a7ec89555c49dc36 ERA-I: http://apps.ecmwf.int/datasets/data/interim_full_daily/?levtype=pl Large-scale forcing: http://johnson.atmos.colostate.edu/dynamo/products/gridded/index.html Gan rawinsonde data: archive.arm.gov (datastream gansondewnpnM1.b1) S-PolKa data: data.eol.ucar.edu/codiac/dss/id=347.017 or contact authors. Gan CombRet heating rates: www.arm.gov/data/pi/71

References

Adames, Á., and J. M. Wallace (2014a), Three-dimensional structure and evolution of the MJO and its relation to the mean flow, *J. Atmos. Sci.*, *71*, 2007–2026.

Adames, Á., and J. M. Wallace (2014b), Three-dimensional structure and evolution of the vertical velocity and divergence fields in the MJO, *J. Atmos. Sci.*, *71*, 4661–4681.

Barnes, H. C., and R. A. Houze Jr. (2013), The precipitating cloud population of the Madden-Julian Oscillation over the Indian and west Pacific oceans, *J. Geophys. Res. Atmos.*, *118*, 6996–7023, doi:10.1002/jgrd.50375.

Benedict, J. J., and D. A. Randall (2007), Observed characteristics of the MJO relative to maximum rainfall, *J. Atmos. Sci.*, *64*, 2332–2354.

Bladé, I., and D. L. Hartmann (1993), Tropical intraseasonal oscillations in a simple nonlinear model, *J. Atmos. Sci.*, *50*, 2922–2939.

Charney, J. G., and A. Elliasen (1964), On the growth of the hurricane depression, *J. Atmos. Sci.*, *21*, 69–75.

Chu, P. S., and J. Wang (1997), Tropical cyclone occurrences in the vicinity of Hawaii: Are the differences between El Niño and non-El Niño years significant?, *J. Clim.*, *10*, 2683–2689.

Ciesielski, P. E., et al. (2014), Quality-controlled upper-air sounding data set for DYNAMO/CINDY/AMIE: Development and corrections, *J. Atmos. Oceanic Technol.*, *31*, 741–764.

Dee, D. P., et al. (2011), The ERA-Interim reanalysis: configuration and performance of the data assimilation system, *Q. J. R. Meteorol. Soc.*, *137*, 553–597.

DePasquale, A., C. Schumacher, and A. Rapp (2014), Radar observations of MJO and Kelvin wave interactions during DYNAMO/CINDY2011/AMIE, *J. Geophys. Res. Atmos.*, *119*, 6347–6367, doi:10.1002/2013JD021031.

Derbyshire, S. H., I. Beau, P. Bechtold, J.-Y. Grandpeix, J.-M. Piriou, J.-L. Redelsperger, and P. M. M. Soares (2004), Sensitivity of moist convection to environmental humidity, *Q. J. R. Meteorol. Soc.*, *130*, 3055–3079.

Dixon, M. (2005), TITAN users' guide, National Center for Atmospheric Research. [Available at http://www.ral.ucar.edu/projects/titan/docs/TitanDataFlow.pdf.]

Dixon, M., and G. Wiener (1993), TITAN: Thunderstorm Identification, Tracking, Analysis, and Nowcasting—A radar-based methodology, *J. Atmos. Oceanic Technol.*, *10*, 785–797.

Feng, Z., S. A. McFarlane, C. Schumacher, S. Ellis, and N. Bharadwaj (2014), Constructing a merged cloud-precipitation radar data set for tropical clouds during the DYNAMO/AMIE experiment on Addu Atoll, *J. Atmos. Oceanic Technol.*, *31*, 1021–1042.

Gottschalck, J., P. E. Roundy, C. J. Schreck III, A. Vintzileos, and C. Zhang (2013), Large-scale atmospheric and oceanic conditions during the 2011–2012 DYNAMO field campaign, *Mon. Weather Rev.*, *141*, 4173–4196.

Haertel, P., K. Straub, and A. Budsock (2014), Transforming circumnavigating Kelvin waves that initiate and dissipate the Madden-Julian Oscillation, *Q. J. R. Meteorol. Soc.*, *776*, doi:10.1002/qj.2461.

Hendon, H. H. (1986), Stream function and velocity potential representation of equatorially trapped waves, *J. Atmos. Sci.*, *43*, 3038–3042.

Hohenegger, C., and B. Stevens (2013), Preconditioning deep convection with cumulus congestus, *J. Atmos. Sci.*, *70*, 448–464.

Hsu, H.-H., B. J. Hoskins, and F.-F. Jin (1990), The 1985/86 intraseasonal oscillation and the role of the extratropics, *J. Atmos. Sci.*, *47*(7), 823–839.

Huffman, G. J., R. F. Adler, D. T. Bolvin, G. Gu, E. J. Nelkin, K. P. Bowman, Y. Hong, E. F. Stocker, and D. B. Wolff (2007), The TRMM multisatellite precipitation analysis: Quasi-global, multiyear, combined-sensor precipitation estimates at fine scale, *J. Hydrometeor.*, *8*(1), 38–55.

Jensen, M. P., and A. D. Del Genio (2006), Factors limiting convective cloud top height at the ARM Nauru Island climate research facility, *J. Clim.*, *19*, 2105–2117.

Johnson, R. H., and P. E. Ciesielski (2013), Structure and properties of Madden-Julian Oscillations deduced from DYNAMO sounding arrays, *J. Atmos. Sci.*, *70*, 3157–3179.

Johnson, R. H., J. H. Ruppert Jr., and M. Katsumata (2015), Sounding-based thermodynamic budgets for DYNAMO, *J. Atmos. Sci.*, *72*, 598–622, doi:10.1175/JAS-D-14-0202.1.

Kemball-Cook, S. R., and B. C. Weare (2001), The onset of convection in the Madden-Julian Oscillation, *J. Clim.*, *14*, 780–793.

Kiladis, G. N., K. H. Straub, and P. T. Haertel (2005), Zonal and vertical structure of the Madden-Julian oscillation, *J. Atmos. Sci.*, *62*, 2790–2809.

Klotzbach, P. J. (2010), On the Madden-Julian Oscillation–Atlantic hurricane relationship, *J. Clim.*, *23*, 282–293.

Klotzbach, P. J. (2014), The Madden-Julian Oscillation's impacts on worldwide tropical cyclone activity, *J. Clim.*, *27*, 2317–2330.

Knutson, R. R., and K. M. Weickmann (1987), 30–60 day atmospheric oscillations: Composite life cycles of convection and circulation anomalies, *Mon. Weather Rev.*, *115*, 1406–1436.
Kumar, V., A. Protat, P. T. May, C. Jakob, G. Penide, S. Kumar, and L. Davies (2013), On the effects of large-scale environment and surface conditions on convective cloud characteristics over Darwin, Australia, *Mon. Weather Rev.*, *141*, 1358–1374.
Kumar, V., C. Jakob, and P. T. May (2014), On the atmospheric regulation of the growth of moderate to deep cumulonimbus in a tropical environment, *J. Atmos. Sci.*, *71*, 1105–1120.
Kummerow, C., W. Barnes, T. Kozu, J. Shiue, and J. Simpson (1998), The Tropical Rainfall Measuring Mission (TRMM) sensor package, *J. Atmos. Oceanic Technol.*, *15*, 809–817.
Long, C. N., and D. J. Holdridge (2012), Investigations of possible low-level temperature and moisture anomalies during the AMIE field campaign on Manus Island, ARM Technical Report, DOE/SC-ARM/TR-119. [Available at http://www.arm.gov/.]
Lorenc, A. C. (1984), The evolution of planetary-scale 200 mb divergent flow during the FGGE year, *Q. J. R. Meteorol. Soc.*, *110*, 427–441.
Madden, R. A., and P. R. Julian (1971), Detection of a 40–50-day oscillation in the zonal wind in the tropical Pacific, *J. Atmos. Sci.*, *28*, 702–708.
Madden, R. A., and P. R. Julian (1972), Description of global-scale circulation cells in the tropics with a 40–50 day period, *J. Atmos. Sci.*, *29*, 1109–1123.
Maloney, E. D., and D. L. Hartmann (2000a), Modulation of hurricane activity in the Gulf of Mexico by the Madden-Julian Oscillation, *Science*, *287*, 2002–2004.
Maloney, E. D., and D. L. Hartmann (2000b), Modulation of eastern north Pacific hurricanes by the Madden-Julian Oscillation, *J. Clim.*, *13*, 1451–1460.
Mapes, B. E. (2001), Water's two height scales: The moist adiabat and the radiative troposphere, *Q. J. R. Meteorol. Soc.*, *127*, 2353–2366.
Matthews, A. J. (2008), Primary and successive events in the Madden-Julian Oscillation, *Q. J. R. Meteorol. Soc.*, *134*, 439–453.
Mlawer, E. J., S. J. Taubman, P. D. Brown, M. J. Iacono, and S. A. Clough (1997), RRTM, a validated correlated-k model for the longwave, *J. Geophys. Res.*, *102*, 16,663–16,682.
Powell, S. W., and R. A. Houze Jr. (2013), The cloud population and onset of the Madden-Julian Oscillation over the Indian Ocean during DYNAMO-AMIE, *J. Geophys. Res. Atmos.*, *118*, 11,979–11,995, doi:10.1002/2013JD020421.
Powell, S. W., and R. A. Houze Jr. (2015), Evolution of convective echo top heights observed by TRMM radar over the Indian Ocean and Maritime Continent during DYNAMO, *J. Geophys. Res. Atmos.*, *120*, doi:10.1002/2014JD022934, in press.
Ray, P., and T. Li (2013), Relative roles of circumnavigating waves and extratropics on the MJO and its relationship with the mean state, *J. Atmos. Sci.*, *70*, 876–893.
Ruppert, J. H., Jr., and R. H. Johnson (2015), Diurnally modulated cumulus moistening in the preonset stage of the Madden-Julian Oscillation during DYNAMO, *J. Atmos. Sci.*, *72*, 1622–1647, doi:10.1175/JAS-D-14-0218.1.
Schumacher, C., R. A. Houze Jr., and I. Kraucunas (2004), The tropical dynamical response to latent heating estimates derived from the TRMM precipitation radar, *J. Atmos. Sci.*, *61*, 1341–1358.
Sears, J. M. (2011), Investigating the role of the upper-levels in tropical cyclogenesis, MS thesis, 96 pp., Univ. of Wisconsin–Madison.
Seo, K.-H., and K.-Y. Kim (2003), Propagation and initiation mechanisms of the Madden-Julian Oscillation, *J. Geophys. Res.*, *108*(D13), 4384, doi:10.1029/2002JD002876.
Sobel, A., S. Wang, and D. Kim (2014), Moist static energy budget of the MJO during DYNAMO, *J. Atmos. Sci.*, *71*, 4276–4291.
Straub, K. H. (2013), MJO initiation in the real-time multivariate MJO index, *J. Clim.*, *26*, 1130–1151.
Takayabu, Y. N., S. Shige, W.-K. Tao, and N. Hirota (2010), Shallow and deep latent heating modes over tropical oceans observed with TRMM PR spectral latent heating data, *J. Clim.*, *23*, 2030–2046.
Ventrice, M. J., M. C. Wheeler, H. H. Hendon, C. J. Schreck III, C. D. Thorncroft, and G. N. Kiladis (2013), A modified multivariate Madden-Julian Oscillation index using velocity potential, *Mon. Weather Rev.*, *141*(12), 4197–4210.
Wang, S., and A. H. Sobel (2012), Impact of imposed drying on deep convection in a cloud-resolving model, *J. Geophys. Res.*, *117*, D02112, doi:10.1029/2011JD016847.
Wheeler, M. C., and K. M. Weickmann (2001), Real-time monitoring and prediction of modes of coherent synoptic to intraseasonal tropical variability, *Mon. Weather Rev.*, *129*, 2677–2694.
Yanai, M., S. Esbensen, and J.-H. Chu (1973), Determination of bulk properties of tropical cloud clusters from large-scale heat and moisture budgets, *J. Atmos. Sci.*, *30*, 611–627.
Yanai, M., J.-H. Chu, T. E. Starx, and T. Nitta (1976), Response of deep and shallow tropical maritime cumuli to large-scale processes, *J. Atmos. Sci.*, *33*, 976–991.
Yoneyama, K. (2003), Moisture variability over the tropical western Pacific Ocean, *J. Meteorol. Soc. Japan*, *81*(2), 317–337.
Yoneyama, K., C. Zhang, and C. N. Long (2013), Tracking pulses of the Madden-Julian Oscillation, *Bull. Am. Meteorol. Soc.*, *94*, 1871–1891.
Yuan, J., and R. A. Houze Jr. (2013), Deep convective systems observed by A-Train in the tropical Indo-Pacific region affected by the MJO, *J. Atmos. Sci.*, *70*, 465–486.
Zhang, C. (2005), Madden-Julian oscillation, *Rev. Geophys.*, *43*, RG2003, doi:10.1029/2004RG000158.
Zhao, C., T. Li, and T. Zhou (2013), Precursor signals and processes associated with MJO initiation over the tropical Indian Ocean, *J. Clim.*, *26*, 291–307.
Zuidema, P. (1998), The 600–800-mb minimum in tropical cloudiness observed during TOGA COARE, *J. Atmos. Sci.*, *55*, 2220–2228.
Zuluaga, M. D., and R. A. Houze Jr. (2013), Evolution of the population of precipitating convective systems over the equatorial Indian Ocean in active phases of the Madden-Julian Oscillation, *J. Atmos. Sci.*, *70*, 2713–2725.

Erratum

In the originally published version of this article, there were minor typographical errors in Equations 2 and 3. These errors have since been corrected and this version may be considered the authoritative version of record.